# NEURAL NETWORK FOR FAST CALCULATION OF THE BOOTSTRAP CURRENT

**Arsene Stéphane Tema Biwolé**

A thesis presented for the degree of
Master of Science


Politecnico di Torino
Department of Energy
Advisors:
Prof. Fabio Subba
Dr. Sterling Smith
Dr. Orso Meneghini
July 2018

# Dedication

***Dedico questi lavori sull'energia a mia madre, l'energia della mia vita.***

# Acknowledgments

I would first like to thank my thesis advisor Professor Fabio Subba. He offered me the opportunity to work on my master thesis abroad in one of the main Tokamak experiments in the World. I am also grateful to him for revising my work and for giving useful advices in the writing of the thesis.

I would also like to thank Dr.Sterling Smith and Dr.Orso Meneghini who followed me since the beginning of the thesis and provided me with all the necessary so that I can achieve this work. Without their passionate participation and inputs,this research work could not have being successfull.

I would like to acknowledge Dr.Jeff Candy and Dr.Emily Belli from whom I learned so much about neoclassical transport physics and plasma physics in general. Working and collaborating with experts of our field has been a very rewarding experience.

Finally, I must express my very profound gratitude to my parents and to my wife for providing me with unfailing support and continuous encouragement throughout my years of study and through the process of researching and writing this thesis. This accomplishment would not have been possible without them. Thank you.

Arsene Stéphane Tema Biwolé.

# Contents


**1 Introduction** **6**

**2 The energy challenge and the fusion research** **10**
2.1 The energy challenge . . . . . 10
2.2 The fusion research . . . . . 12
2.2.1 The promising D-T fusion reaction . . . . . 13
2.2.2 The other fusion reactions . . . . . 15

**3 Neoclassical transport and bootstrap current in tokamak plasmas** **16**
3.1 Tokamak reactors . . . . . 16
3.1.1 Drifts . . . . . 16
3.1.2 The DIII-D tokamak at General Atomics . . . . . 19
3.2 Neoclassical transport . . . . . 19
3.2.1 Some definitions . . . . . 21
3.3 Bootstrap current . . . . . 24
3.3.1 The concept of Low and high collisionality . . . . . 25
3.3.2 The physical mechanism behind the bootstrap current . . . . 26

**4 Bootstrap current models and their limitations** **29**
4.1 Definitions . . . . . 29
4.1.1 The Drift-Kinetic Equation DKE . . . . . 29
4.2 The first principle code NEO . . . . . 30
4.3 The Sauter model . . . . . 30
4.4 The KCK12 model . . . . . 31

**5 Neural network approach** **36**
5.1 Neural Networks (NN) generalities . . . . . 36
5.2 Neural network for the bootstrap current . . . . . 38
5.3 Some useful definitions in the framework of Neural Networks . . . . 39
5.4 Algorithm . . . . . 40
5.5 Parametrization . . . . . 41
5.6 Training . . . . . 42

**6 Accuracy of the NN model** **45**

**7 NN prediction of experimental bootstrap current profiles** **50**
7.1 DIII-D . . . . . 50
7.2 JET . . . . . 52
7.3 ITER and the future tokamak reactors . . . . . 52

**8 Applications of the new bootstrap current calculation** **55**
8.1 Implications for MHD equilibrium reconstructions . . . . . 55
8.1.1 The Grad–Shafranov equation . . . . . 55

**9 Conclusion** **60**

# Chapter 1

# Introduction

*To Bring a Star to Earth* is the goal of Fusion Energy research.
All the stars , including our Sun are powered by nuclear fusion reactions that take place in their core. Nuclear fusion reactions, like nuclear fission reactions release energy according to the mass-energy equivalence formula discovered by *Albert Einstein* in 1905:

$$E = mc^2 \tag{1.1}$$

Where $m$ is the mass, $E$ the energy and $c$ is the speed of light.
In the case of nuclear fusion reactions, two or more light nuclei fuse together to form one or more different nuclei and subatomic particles ( neutron and protons).The mass difference between the reactants and the products is transformed in energy with a factor equal to the square of the speed of light ($\approx 9 \times 10^{16}\ m^2/s^2$).
Since several decades, fusion energy as a possible energy source on earth has seriously been under studies, not only for the important amount of energy released in each reaction, but also for the fact that the fuel for this energy source would be practically inexhaustible. In our Sun, fusion is achieved by hydrogen nuclei that fuse into helium.The gravity in the Sun compresses the particles and enhance the fusion reaction.On Earth it is not possible to build a machine with such a huge mass as the Sun to confine particles by gravity for fusion. This is the reason why research focuses on two types of confinement, the inertial confinement and the magnetic confinement. To understand those two techniques let's first remember that in order to achieve fusion on Earth, particles have to be heated at very high temperature (about 10 times the temperature in the core of the Sun). The particles are then in a state called *plasma* where atoms are freed from their electrons.The plasma is known as the fourth state of matter, the others being solid, liquid and gas. The fact that the plasma is a mixture of ions and electrons has given an idea to physicists for their confinement. In fact charged particles in a magnetic field experience the Lorentz force and gyrate around the magnetic field lines.The idea of magnetic confinement reside in creating a magnetic field in a toroidal geometry to keep plasma particles confined and increase the probability they will collide and fuse together. The other option, the inertial confinement, consists in heating and compressing a fuel target in the form of a pellet that contains a mixture of light nuclei (typically deuterium and tritium). The magnetic confinement is believed to be the most promising path toward achieving fusion and there are many experiments in the world implementing this strategy. Many of these experiments are of the so-called "Tokamak" type, on which this thesis focuses. This thesis work has been carried out on the DIII-D

tokamak situated in San Diego , California.
Tokamak machines are devices with torus geometry in which two magnetic fields are superimposed to enclose the plasma. A toroidal field generated by external coils and a poloidal field generated by a current flowing in the toroidal direction inside the plasma. This plasma current has the two purposes of creating a poloidal magnetic field and to heat the plasma.The plasma current is typically driven externally,this is done through a transformer coil which induces current inside the plasma. In principle, a time varying current is generated in the primary winding of the transformer so that a current is driven in the plasma, which is the secondary circuit (see Fig.1.1). The increasing current in the primary winding of the transformer can be generated only for a limited amount of time, this is why tokamaks do not work in continuous but in pulse mode. The plasma current also can be driven through a neutral-beam current drive method. The method consists in a beam of high-energy neutral atoms which is injected into the plasma along the toroidal direction. The neutral beam will freely enter the plasma since it is unaffected by the magnetic field. The neutral atoms become ionized by collisions with the electrons. The beam then consists of energetic positively charged nuclei that are confined within the plasma by the magnetic field. The high-speed ions travel toroidally along the magnetic field and collide with the electrons, pushing them in one direction and thereby producing a current (Fig. 1.2).
There is a particular component of the plasma current which adds to the ones we described above.This component is called the *Bootstrap Current* and has been experimentally observed for the first time by *Michael C. Zarnstorff* working in his PhD thesis (*Experimental Observation of Neoclassical Currents*)[1]. The motivations for our research work come from this experimentally observed current which arises naturally in tokamak plasmas every time there is particle density and temperature gradient.The discovery of this current was so stimulating because it opened the opportunity for the study and the development of a steady-state fusion reactor.In fact, the low efficiency of the methods for driving the current inside the plasma and the large cost associated to external current drive system has generated interest in the study of the bootstrap current. Moreover, in magnetic confinement fusion research, an important topic is the macroscopic plasma behaviour, i.e. how it can reach an equilibrium and stability in toroidal geometry, considering all the macroscopic forces that act on it. This field that looks at a plasma as a fluid is called MHD (MagnetoHydroDynamics), and MHD studies plasma equilibrium and stability. The bootstrap current has been observed to be an important part of the total current in the plasma (especially in the edge region of the tokamak where it can make up to 70% to 90% of the total current)[1][2], it then plays a crucial role on MHD analysis. Those analysis are performed sometimes integrating together many codes, dealing with different physics aspects , this is what we refer to as integrated modelling.For integrated modelling, fast and accurate calculation of the bootstrap current is fundamental in order to study its implication on the plasma stability and equilibrium.
All this environment was already set before I arrived at General Atomics for this thesis work, and our mission was to provide a fast and accurate formula to calculate the bootstrap current. The first step was to understand how the current is presently calculated.The two most popular calculation methods both have a drawback. The first one is based on a computer simulation code called NEO [3],it gives accurate

result but is CPU demanding and consequently slow. The other option for calculating the bootstrap current is the world-wide used Sauter analytic formula [4][5], which is faster; the issue with the formula is that it is not accurate at all plasma regimes[2][6]. The challenging goal we had was to develop a method to compute the bootstrap current which should ideally be as fast as the Sauter model and as accurate as the NEO simulation code. Our idea was to try and build a formula that rely on artificial neural networks or simply neural networks (NN) [7]. Neural networks are specific algorithms in the field of machine learning that in the past have been successfully used for critical physics issues. They have been used for example to predict turbulent transport fluxes in tokamak plasmas [8]. What is the most interesting about neural networks is that they are capable of breaking the speed-accuracy trade-off that is expected in traditional physics models, and this definitely convinced us to rely on NNs to build our formula. The remainder of this thesis will provide in detail all the steps of our work and the important results we obtained. The structure is as follows:
In Chap. 2, an overview of nuclear fusion research and the world energy challenge is given.The following chapter (Chap. 3 ) starts first by describing the principles of a tokamak reactor and then explains the neoclassical component of the transport in tokamak plasmas and one of its most important effects: the bootstrap current. Chap. 4 describes more deeply the neoclassical bootstrap current, highlighting the actual bootstrap current models and their limitations. At the end of this chapter, one might understand why a new bootstrap current model is needed and also by looking at the unsuccessful previous models why this work had to be thoughtfully done. Chap. 5 and Chap. 6 present the Neural Network (NN) approach to calculate the bootstrap current. The accuracy of our physics model is also discussed. Chap. 7 naturally follows showing the NN prediction of experimental bootstrap current profiles. This exercise has been done not for present tokamak machines only; an extrapolation to future tokamak devices is also discussed.This is possible since we developed a formula that can be extended to other fusion devices, and to any impurity species, not only carbon impurity as in DIII-D simulations. The new calculation of the bootstrap current, which offers an important improvement to prior models, has several applications; those are presented in Chap. 8. Finally, all the results obtained in this work are highlighted in the Conclusion with a summary of all the applications of our work and the relevance for the ITER machine.

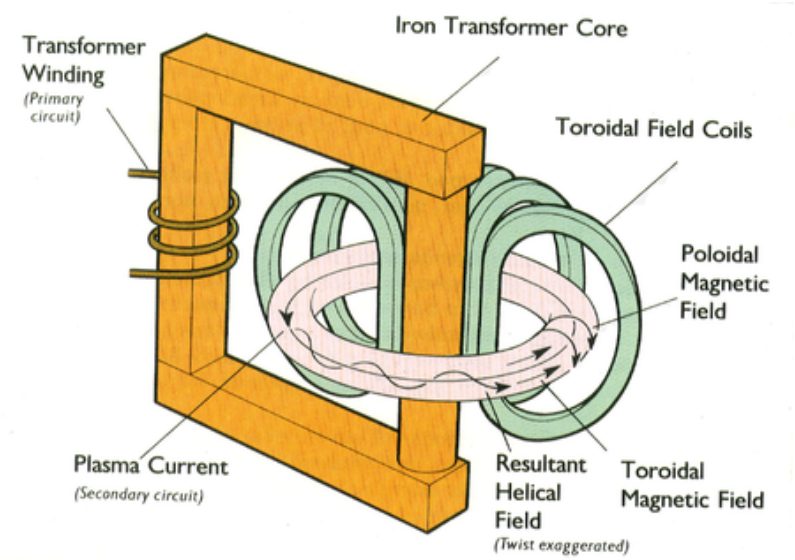


Figure 1.1: Principle of a tokamak reactor. The plasma is the secondary of the transformer circuit.
Source: *Max-Planck-Institut fur Plasmaphysik.*

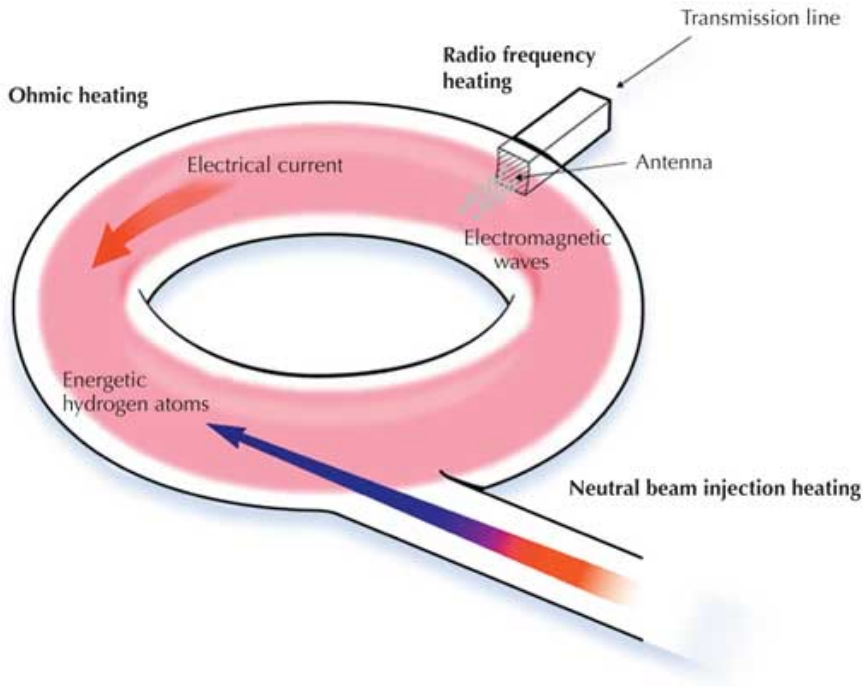


Figure 1.2: Illustration of a Neutral Beam Injection.
Source: *The European journal for science teachers.*

# Chapter 2

# The energy challenge and the fusion research

## 2.1 The energy challenge

How can the world continue to develop, and poor countries continue to grow, without excessive costs — whether financial or environmental?
One-third of the world's population use organic material, like wood or charcoal for cooking, heating, and lighting. This has the consequence of high levels of indoor air pollution and a considerable increase in the incidence of respiratory infections: pneumonia, tuberculosis, chronic obstructive pulmonary disease, etc. This leads to up to 2.5 million premature deaths each year, mostly women and children according to the World Health organization.Figure 2.1 illustrates a typical cooking time in an average home in a poor country.The family will absorb particulates because they will spend the most of the time in the kitchen, using fire sometime also for heating purposes during the night. Figure 2.2 shows a comparison of the relative harm of different energy sources in developing country, biomass by air pollution is causing the most damage. It is interesting though to stress the fact that the families that use biomass mainly do not have access to electricity. This leads to an important challenge in those countries, the challenge of having a clean and affordable energy source.

On the other hand Urbanization and Industrialization have always seemed to be the key to wealth and better living, but in reality, it has been shown that, although it leads to better conditions of living, it affects our environment by air pollution and ultimately also contributes to climate change[9]. An example is illustrated in figure 2.3, which shows several hundreds of deaths in a single pollution event in London due to a high concentration of $SO_2$ in the atmosphere. This pollution event in London is known as the great smog of London. It started in early December 1952, a period of cold weather.Airborne pollutant arising mainly from the use of coal was collected by an anticyclone and windless conditions to form a thick layer of smog over the city.It lasted from Friday 5, to Tuesday 8 December 1952 and caused more than 10 000 death in England. Figure 2.3 shows the trend of the damage during the days the pollution reached its pick, on the picture we clearly see how the damages(deaths) are linked to the pollutant concentration.

In this situation we understand better why the environmental challenge is important and so also the energy challenge both in developed and in developing coun-

Figure 2.1: Developing country biomass use generates indoor particulates.
Source: World Health Organization Picture: Practical action

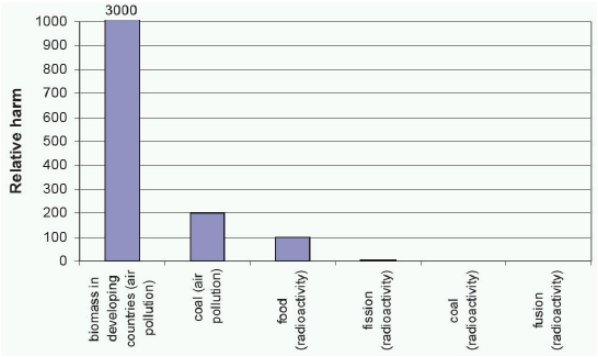


Figure 2.2: Relative harm of biomass (fuel) in developing countries

tries.Especially given the fact that the growth in energy use is enormous.In fact there are two characteristic regions of the world: near saturated energy demand and dramatically growing energy demand. Recently, just the growth in Chinese consumption has equaled the total German consumption.

Figure 2.4 shows how the situation is changing with respect to the past where energy use was mainly dominated by OECD countries (with $< 20\%$ of the global population).

The growing energy demand has to be met in an economically feasible and environmentally friendly way. The issues associated with the emission of greenhouse gases motivate one to not push on the use of coal and fossil fuels as energy sources.

A possible solution could be to increase the production of actual carbon-free energy (nuclear fission, solar panels, wind, etc.). This solution still will not be convenient in the long term because of the non negligible issues associated with radioactive wastes or low and variable production from renewable sources. This has been the motivation toward the research of unlimited, eco-friendly, and economically achievable source of energy . This new source will be integrated in the actual energy

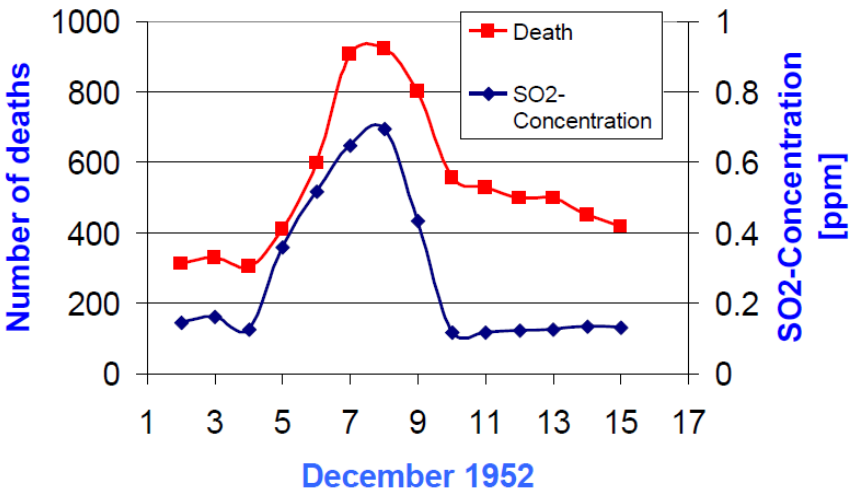


Figure 2.3: Example pollution event in London
Source: Wilkins

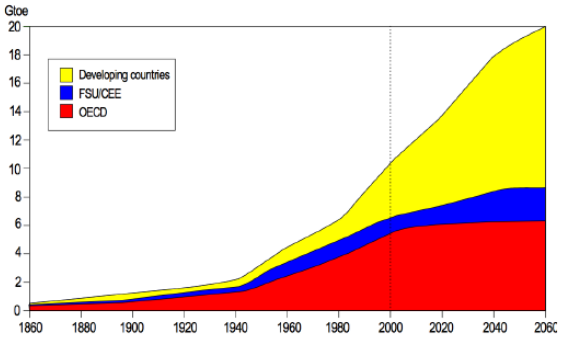


Figure 2.4: Predicted energy growth
Source: World Energy Council,World Bank

mix.

## 2.2 The fusion research

Fusion research aims at using as an energy source the energy from the nuclear fusion of two light nuclei. Like nuclear fission, nuclear fusion produces energy from a nuclear reaction according to the Einstein relation $E = mc^2$ . In fact what is important is how tightly the protons and neutrons are held together. If a nuclear reaction produces nuclei that are more tightly bound than the originals then energy will be produced. It turns out that the most tightly bound atomic nuclei are around the size of iron (with 26 protons in the nucleus). That is, one can release energy either by splitting very large nuclei like uranium with 92 protons to get smaller products (nuclear fission) or fusing very light nuclei like hydrogen with just one proton to get bigger products (nuclear fusion). In both cases the reaction shifts the size of the atoms involved towards iron, that is towards lower energies in the “valley” pictured

below. The energy gain is released in the form of kinetic energy of the products of the reaction which is then converted to heat.

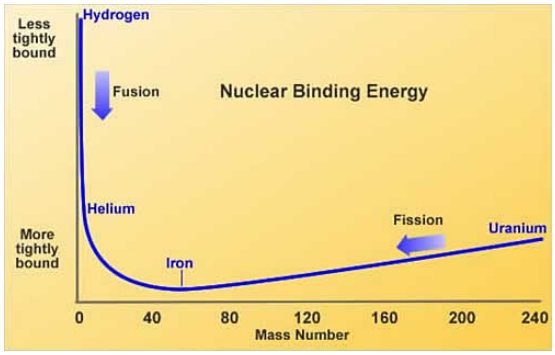


Figure 2.5: Nuclear binding energy
Source: EUROfusion

A particularly interesting fusion reaction is the reaction between deuterium and tritium, which are isotopes of hydrogen. Deuterium has a natural abundance in Earth's oceans of about one atom in 6420 of hydrogen, and so can be considered as a limitless resource. Tritium, on the other hand, is a radioactive isotope of hydrogen; naturally occurring tritium is extremely rare on Earth but can be produced during the following nuclear reactions.

$$^{6}Li + n \longrightarrow T + \alpha + 4.8Mev \tag{2.1}$$

$$^{7}Li + n \longrightarrow T + \alpha + n - 2.5Mev \tag{2.2}$$

Naturally, Lithium contains about 7.4% of $^{6}Li$ and 92.6% of $^{7}Li$. Nevertheless the reaction involving Lithium 6 is the easier. Tritium then can be produced using that reaction. It is important to notice that this reaction can happen directly in the blanket surrounding the region where the fusion reaction is happening. In this way the blanket will be the supplier of Tritium; this is the concept of the breeding blanket in fusion research. The availability of $^{6}Li$ and Deuterium ($D$) confirm that fusion energy has the potential to provide a very long-term energy supply, all with less damage to the environment (i.e. no greenhouse gases, almost no $CO_2$ emission, and most importantly no radioactive wastes — as an example the product of the fusion reaction between deuterium and tritium is Helium-4 and a neutron. Helium-4 is non-radioactive isotope of the element Helium). It is interesting now to discuss another very important characteristic of fusion reactions. Unlike the nuclear fission reaction where an uncontrolled chain reaction can start, fusion (in a fusion reactor) is in that sense stable. In fact fusion reactions need heat to occur. In case of an accident on a fusion reactor, without another huge supply of heat, the reactions will automatically stop without any possibility of an uncontrolled chain reaction.

### 2.2.1 The promising D-T fusion reaction

Let's discuss in detail the fusion reaction between Deuterium and Tritium to understand its feasibility in an actual reactor and the amount of energy involved . The D-T reaction is

$$D + T \longrightarrow \alpha + n + 17.6Mev \tag{2.3}$$

$\alpha$ is the Helium-4 isotope we mentioned above. The energy comes from the mass difference ($\Delta$m) between reactants and products.

$$\Delta m = m(D) + m(T) - m(\alpha) - m(n)$$

$$\Delta m = m({}_1H^2) + m({}_1H^3) - m({}_2He^4) - m({}_0n^1)$$

According to Ref. [10]:

$$\Delta m = 2.014102 + 3.016050 - 4.002603 - 1.008665$$

So, $\Delta m = 0.018884$ a.m.u. [10] are converted to energy for every nucleus of deuterium (or tritium) that fuse. Therefore,

$$\begin{aligned}
\Delta E &= \Delta m c^2 \\
&= (0.018884 a.m.u)(\frac{1.66056 \times 10^{-27} kg}{1 a.m.u})(3 \times 10^8 \frac{m}{s})^2 \\
&= (2.82 \times 10{-}12J)(\frac{6.242 \times 10^{12} MeV}{1J}) \\
&= 17.6 MeV/nucleus
\end{aligned}$$

The D-T reaction is not the only interesting one as far as the produced energy is concerned. Under study are also D-D (deuterium-deuterium) reactions and D-He-3 (deuterium-helium-3) reactions. The issue with the other two reactions is the initiation — the temperature required to initiate is much higher than the one required in the D-T reaction. This is clear looking at Fig. 2.6.

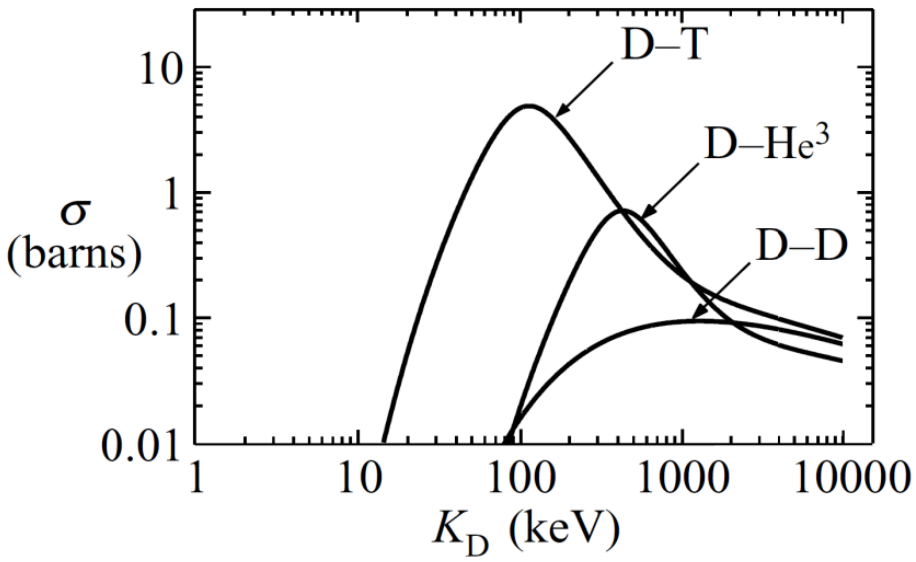


Figure 2.6: Experimentally measured cross sections for the D-T,D-$^3$He, and D-D fusion reactions as a function of deuteron energy $k_D = m_D v_D^2/2$. The cross section of the D-T reaction is the highest at low energies (close to 100 keV). [8, 11]

Figure 2.6 illustrates how hot the given mixture of D/T should be to allow fusion to occur (hundreds of millions of degrees). This is even hotter than the temperature in the core of the sun. The hot gas mixture here is in plasma state.

### 2.2.2 The other fusion reactions

Under studies there is also the fusion of helium-3 as a future energy source. helium-3 is a light , non- radioactive isotope of helium with two protons and one neutron. It has the important property that his fusion will release large amount of energy without causing the surrounding material to become radioactive. The issues associated with helium-3 are mainly that it requires higher temperatures for fusion, and that its abundance is thought to be greater in the moon than in the Earth. Here are summarized the different fusion reactions, it is important to observe also the number of neutrons produces.

$$D + D \longrightarrow^3 He + n + 3.268Mev \tag{2.4}$$

$$D + T \longrightarrow^4 He + n + 17.571Mev \tag{2.5}$$

$$D +^3 He \longrightarrow^4 He + p + 18.354Mev \tag{2.6}$$

# Chapter 3

# Neoclassical transport and bootstrap current in tokamak plasmas

## 3.1 Tokamak reactors

Understanding the neoclassical transport physics starts by studying tokamak reactors principles. Tokamak reactors use the magnetic confinement fusion principle, which is the approach to generate the fusion power using magnetic field to confine the hot fusion plasma. The other approach, the inertial confinement fusion is beyond the scope of this thesis work. To have a good view of the magnetic confinement principles we should first focus our attention on the very basic principle of the motion of a charged particle in a magnetic field. If a charged particle of charge q with velocity $\vec{v}$ is introduced in a magnetic field $B$, it experiences the Lorentz force:

$$\vec{F} = q\vec{v} \times \vec{B}. \tag{3.1}$$

The Lorentz force which is both perpendicular to the magnetic field direction and the velocity of the particle constrains the particles to gyrate around the magnetic field lines. The spiral motion around the magnetic field lines has inspired plasma physicists in the design of the tokamak. The tokamak (an acronym from the Russian words for toroidal magnetic confinement) consist in a doughnut-shape device with magnetic field line winding hellicaly around the torus. This configuration allows the particle that gyrate around the field lines, to be confined inside the torus. The Tokamak for its properties, is believed to be the most promising solution for using fusion energy in the future. The geometry allowing this is a torus shown in figures 3.1a, 3.1b taken from [8]. $R$ and $z$ are the radial and vertical coordinates of the torus; $R_0$ is the major radius and $a$ the minor radius; the plasma section plane parallel to the $R$,$z$ plane is called the *poloidal* plane and the angle $\theta$ is the poloidal angle; $\Phi$ is the toroidal angle.

### 3.1.1 Drifts

The particles, travelling with a spiral motion in the toroidal direction experience motions drifts that push them outward and so they are not well confined [12]. In

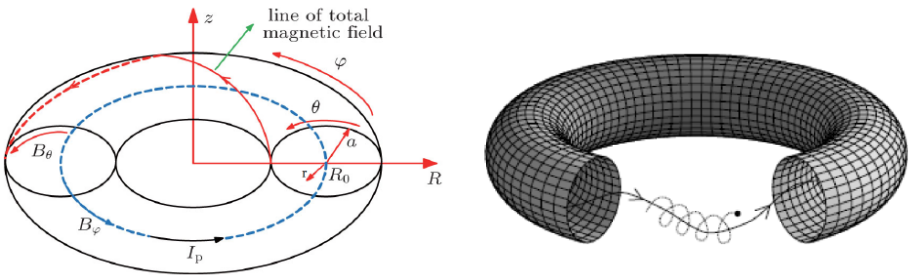


(a) (b)

Figure 3.1: Toroidal coordinates definition and magnetic field components representation 3.1a. Charged particle orbit in dashed line in a toroidal magnetic field (continuous line) 3.1b. [8]

this section we will enumerate the different drifts particles are subject to during their motion around the magnetic field lines.

### E x B Drift

Considering a charged particle moving in a system with a uniform magnetic field $B$ and a uniform electric field $E$ which is in the direction perpendicular to the local magnetic field $B$. If this particle has no velocity component parallel to the local magnetic field and magnetic momentum of this particle is conserved, then its velocity is found to be the sum of its gyro motion velocity a time independent guiding center drift velocity.

$$\vec{v} = \vec{v_{gyro}} + \vec{v_{drift}}. \tag{3.2}$$

$\vec{v_{drift}}$ is found to be :

$$\vec{v_{drift}} = \frac{\vec{E} \times \vec{B}}{B^2} \tag{3.3}$$

It is important to notice that in this case the direction of the guiding center drift velocity do not depend on the sign of the charged particle.

### Gravitational Drift

The gravitational is a generalization of the previous drift. If we consider a charged particle moving in a system with a uniform magnetic field $\vec{B}$ and a uniform gravitational field $\vec{g}$ which is again perpendicular to the local magnetic field, then the guiding speed drift is found to be equal to :

$$\vec{v_{drift}} = \frac{m\vec{g} \times \vec{B}}{qB^2} \tag{3.4}$$

Drift speed of gravitational drift increases with increasing particle's mass.

### Curvature Drift

Considering a charged particle with constant magnetic moment and non-zero velocity component parallel to the local magnetic field. If curvature of the magnetic field

line is non-zero and $R_B$ is the radius of curvature, then the particle experience a curvature drift:

$$\vec{v_{drift}} = \frac{mv_{\parallel}^2}{qB^2}(\frac{\vec{R_B}}{R_B} \times \vec{B}) \tag{3.5}$$

Drift speed of the curvature drift increases with increasing $mv_{\parallel}^2$ (which is proportional to particle's kinetic energy in the direction parallel to local magnetic field).

### Grad B Drift

Now considering a charged particle moving in a system with non-uniform magnetic field $\vec{B}(r)$. If the non-uniformity of the magnetic field is small enough such that we can use the first two terms in Taylor expansion to estimate magnetic field based on magnetic field information at guiding center of the charge particle. The we still can decompose the velocity of this particle into sum of the gyration velocity and a guiding center drift, in this case the drift velocity is expressed as :

$$\vec{v_{drift}} = \frac{mv_{\perp}^2}{2qB}\frac{(-\nabla_{\perp}B) \times \vec{B}}{B^2} \tag{3.6}$$

In this case, the grad-B drift speed increases with increasing perpendicular kinetic energy.

### Polarization Drift

This drift arises when the charged particle is in a system where the electric field is not constant anymore. for instance where $\vec{E} = \vec{y}E(t)$ and $\vec{B} = \vec{z}B$. The total velocity here is written as :

$$\vec{v}(t) = \vec{v}_{gyro}(t) + \vec{v}_{ExB}(t) + \vec{v}_{Polarization} \tag{3.7}$$

we then find the guiding center drift velocity as:

$$\vec{v}_{Polarization} = \vec{y}\frac{m\dot{E}(t)}{qB^2} \tag{3.8}$$

Polarization drift can result in polarization current

The drifts we enumerated are an issue to the confinement, however if the magnetic lines are twisted, the drifts can be neutralized. In a tokamak the twisting is done by inducing a plasma current in the toroidal direction, which generates a poloidal magnetic field see figure 3.2. in the other hand the toroidal magnetic field is produced by coils that surround the toroidal vacuum chamber containing the plasma (see figure 3.3), in those coils flows current and the research is oriented towards superconducting field coils.

Typically in a tokamak machine the magnitude of the toroidal field is greater than the poloidal one $B_{\Phi} > B_{\theta}$.

Now, The plasma current is normally induced by a transformer coil. This is why a tokamak does not work in continuous, but in pulsed mode: In a transformer it is only for a limited time that an increasing current can be generated in the primary winding so that a current can be driven in the plasma. The transformer must, then

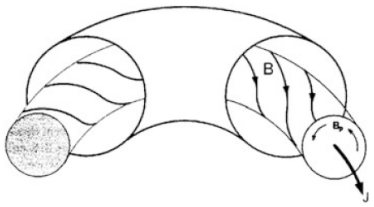


Figure 3.2: The toroidal plasma current $J$ induces the poloidal field component $B_p$. The sum of toroidal and poloidal magnetic field results in the helical magnetic field B (twisted).[12]

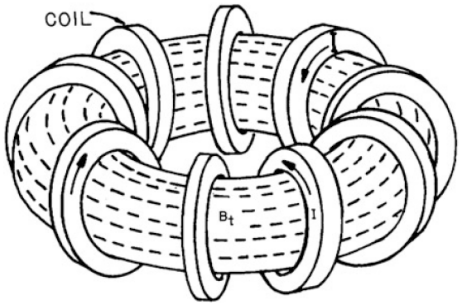


Figure 3.3: A toroidal magnetic field. The magnet coil currents, I, create a toroidal magnetic field, $B_t$ (dashed lines). [13]

be "discharged" and the current started up afresh. In order to achieve steady state operation in a future tokamak power plant, investigations are being conducted on methods of generating current in continuous mode, e.g. by means of high-frequency waves.

### 3.1.2 The DIII-D tokamak at General Atomics

This master thesis has been done at the DIII-D National Fusion Facility, at General Atomics.DIII-D is the largest magnetic fusion research experiment in the United States and one of the main operating tokamaks in the World.with a program mission to establish the scientific basis for the optimization of the tokamak approach to fusion energy production. DIII-D is an evolution of the earlier Doublet I and Doublet II experiments, where doublet is a two lobed toroidally symmetric plasma shape configuration. a picture of Doublet 2 is shown in figure 3.4. DIII-D started operating in 1978, and stopped in 1986 for a major upgrade, and restarted again in 1986. Main DIII-D parameters are summarized in table 3.1.

## 3.2 Neoclassical transport

We described how fusion works and where we want to achieve fusion: in a tokamak device. In that machine there is transport of particles, momentum, and heat. In this section we will focus on the neoclassical component of the the total transport

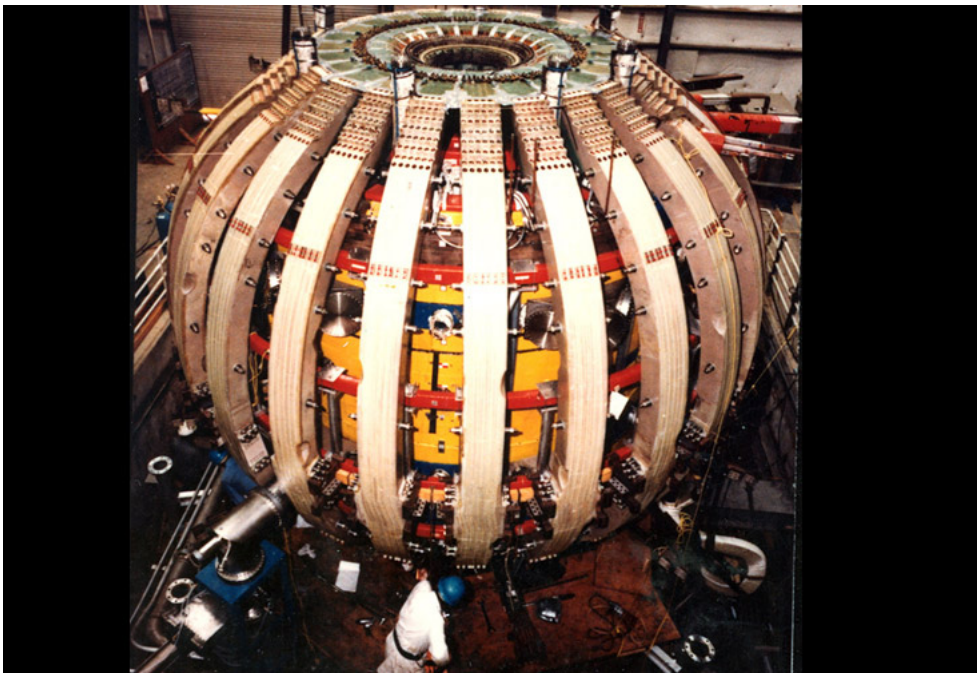

Figure 3.4: A picture of the Historical Doublet II magnetic confinement machine in San Diego (General Atomics)

| | |
|---|---|
| Major radius $R_0$ | $1.67m$ |
| Minor radius $a$ | $0.67m$ |
| Maximum plasma current $I_p$ | $3MA$ |
| Maximum toroidal field $B_\Phi$ | $2.2T$ |
| Available Ohm magnetic flux | $10.5Vs$ |
| Heating | $23MW$ |
| Wall | Carbon |

Table 3.1: Main DIII-D parameters

process in a tokamak.

**Interesting historical fact**

The pioneers of plasma physics and tokamak physics, during the early design of tokamak reactors, believed that the transport would be essentially neoclassical. Neoclassical transport is due to coulomb collisions adapted to a toroidal geometry. Then it happened that during experiments, all of the measured quantities (heat fluxes, temperatures, densities) did not match the theoretically predicted ones. The scientists wondered how were the particles being "transported" — they wondered what the other component of transport in tokamak plasmas was. Later on, we found out that the other component, or actually the main component of the transport is the anomalous transport — the so-called turbulent transport processes, which actually dominate transport phenomena in tokamak plasmas. Even if the neoclassical transport is not the dominant part of the transport in a tokamak, it still is one of the pillars of the physics of magnetically confined plasmas [14],[15].

The neoclassical transport theory provides a model for transport of particles,

momentum, and heat due to Coulomb collisions in confined plasmas and in toroidal geometries. The difference between the classical and neoclassical models lies in the incorporation of geometric effects, which give rise to complex particle orbits and drifts.

The theory starts from the kinetic equation for the particle distribution function $f_\alpha(\vec{x}, \vec{v}, t)$[14] known as the Boltzmann equation:

$$\frac{\partial f_\alpha}{\partial t} + \vec{v} \cdot \nabla f_\alpha + \frac{\vec{F}}{m} \frac{\partial f_\alpha}{\partial t} = C_\alpha(f) + S_\alpha \tag{3.9}$$

where $\alpha$ indicates the particles species, $\vec{v}$ is the velocity, $\vec{F}$ is the Lorentz force (Equation 3.1) acting on the particle. In the next section we will define some useful terms for the understanding of the theory.

### 3.2.1 Some definitions

#### moments

The Boltzmann equation (Eq: 3.9) describes how the phase-space density changes around a particle with time due to collisions .The Boltzmann equation can be used to describe the time-evolution of macroscopic quantities such as density, macroscopic velocity , etc. This is done by considering the moment equations of the Boltzmann equation. In mathematics the $n^{th}$-moment of a real valued, continuous function $f(x)$ is:

$$\mu_n = \int x^n f(x) dx \tag{3.10}$$

So in relation to our analysis we can define the quantity:

$$g(\vec{x}, t) = \int Q(\vec{v}) f_\alpha d^3\vec{v} \tag{3.11}$$

and there are few functions $Q(\vec{v})$ that are for particular interest :
if $Q(\vec{v}) = 1 \longrightarrow g(\vec{x}, t) = n(\vec{x}, t)$, zeroth-order moment.
if $Q(\vec{v}) = m\vec{v} \longrightarrow g(\vec{x}, t) = \rho(\vec{x}, t)$, first Order moment. and so forth.

#### Maxwellian distribution function

Another important concept is the normal distribution function or the Maxwellian distribution function. It is defined as :

$$f(\vec{v}) = (\frac{m}{2\pi kT})^{3/2} \exp - \frac{mv^2}{2kT} \tag{3.12}$$

where $m$ is the particle mass and $kT$ is the product pf the Boltzmann constant and thermodynamic temperature . It was first used for describing particle speeds in idealized gases where the system of particle is assumed to have reached the thermal equilibrium.

### Gyroradius

Now we will define what we will refer to as the gyroradius. The gyroradius or the Larmor radius is the radius of the circular motion of a charged particle in the presence of a uniform magnetic field. It is often used as a comparison length for many plasma phenomena. Starting from Equation 3.1; we can derive the larmor radius:

$$r_g = \frac{mv_\perp}{qB} \tag{3.13}$$

where $m$ is the mass of the particle and $v_\perp$ is the component of the velocity perpendicular to the direction of the magnetic field , $q$ is the absolute value of the electric charge of the particle and $B$ the strength of the magnetic field.

### pedestal

We will be using many times the word pedestal in this thesis.The simplest definition we can give is that the pedestal in a high confined tokamak plasma is the region in the edge where steep gradients in the density and temperature are observed. It is an important region for the bootstrap current since the bootstrap current is driven by those gradients.

### MHD equations

The moments we described previously constitute the basics of the fluid theory of the plasma.With respect to fusion research, the fluid model provide a reasonably accurate description of all the important phenomena: macroscopic equilibrium and stability, transport, heating and current drive. From the moments of the Boltzmann equations , we are provided with the conservation equations for each species in the plasma namely the electrons and the ion. This is called the two fluids model. The MHD(Magnetohydrodynamics) model is a reduction of the two-fluid model to a single fluid model derived by focusing attention on the length and time scales characteristic of macroscopic behavior, and defining proper single fluid variables($\rho$,$u$). An important aspect to stress is the fact that while in a single particle theory , the electric field and the magnetic field are prescribed (section o the drifts), MHD is a self-consistent theory including the field created by the moving particles. the summary of MHD equations are :
mass: $\frac{d\rho}{dt} + \rho\nabla \cdot \vec{v} = 0$ ;
momentum : $\rho\frac{d\vec{v}}{dt} = \vec{J} \times \vec{B} - \nabla p$;
Ohm's Law: $\vec{E} + \vec{v} \times \vec{B} = 0$;
energy : $\frac{d}{dt}(\frac{p}{p^\gamma}) = 0$;
Maxwell : $\nabla \times \vec{E} = -\frac{\partial \vec{B}}{\partial t}$; $\nabla \times \vec{B} = \mu_0 J$; $\nabla \cdot \vec{B} = 0$;
$p$ in the momentum equation is the macroscopic pressure, $J$ is the current, $\gamma$ is the heat capacity ratio.

### Flux surfaces

The steady state form of the mometum equation is given by :

$$\vec{J} \times \vec{B} = \nabla p \tag{3.14}$$

This means that $\nabla p$ is perpendicular to both $\vec{J}$ and $\vec{B}$. By definition the vector $\nabla p$ is perpandicular to $p = const.$contours. It then follows that:

$$B \cdot \nabla p = 0 \tag{3.15}$$

The implication is that the magnetic field lines (i.e., the lines parallel to $\vec{B}$) must lie in the surfaces of constant pressure; there is no component of $B$ perpendicular to the surface.Hence, these surfaces are also called flux surfaces. In a confined plasma the pressure and flux contours coincide, forming a set of closed, nested, toroidal surfaces. The concept of flux surface if fundamental in tokamak physics , because the physics of the center of the tokamak can be studied only in one dimension (the radial dimension), since properties are constant in a flux surface.Figure 3.5 shows flux surfaces in a tokamak.

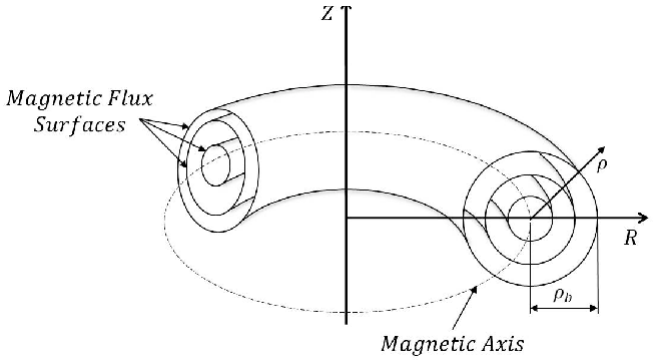


Figure 3.5: Magnetic flux surfaces in a tokamak.

$S_\alpha$ and $C_\alpha$ in Equation 3.9 represent the source and the collision operator. If the chosen collision operator is the Fokker-Planck operator [16], the equation is called the Fokker-Planck equation.Instead the collisionless Boltzmann equation is sometime called the Vlasov equation.

Generally the derivation of this operator is non-trivial and requires making many assumptions. The collision operator must satisfy some obvious conservation laws (conservation of particles, momentum, and energy). Once the collision operator is decided, the moments of the kinetic equation can be computed . if we call $u$ the macroscopic velocity of the moving particles, Theses fluid moments are:
$\vec{n} = \int f d^3\vec{v}$ (particle density)
$\vec{\Gamma} = \int v f d^3\vec{v}$ (particle flux)
$\vec{P} = \int \frac{mv^2}{2}\vec{v} f d^3\vec{v}$ (energy flux)
$\vec{P'} = \int m(v-u)\cdot(\vec{v}-\vec{u}) f d^3\vec{v}$ (pressure tensor) and
$\vec{Q} = \int \frac{m(\vec{v}-\vec{u})^2}{2}(\vec{v}-\vec{u}) f d^3\vec{v}$ (heat flux).
We can give an example of the evolution equation of the first moment , which becomes :

$$\frac{\partial n}{\partial t} + \nabla(nu) = S_n \tag{3.16}$$

The principal goal of the neoclassical theory is to provide a closed set of equations for the time evolution of these moments, for each particle species in the plasma. It is interesting to notice that the determination of any moment requires knowledge of

the next order moment. Usually some assumptions are made in order to facilitate the analysis, for example: small gyroradius, large parallel transport ( with respect to the magnetic field), Maxwellian distribution function, etc. So finally after these assumptions the equations can be restated to reflect the *radial* transport;i.e the transport normal to magnetic flux surfaces and averaged over flux surface. (A flux surface is a given smooth surface $S$ with normal $\vec{n}$ where $\vec{B} \cdot \vec{n} = 0$ everywhere on $S$, in other words, the magnetic field does not cross the surface $S$ anywhere, i.e., the magnetic flux traversing S is zero). We mentioned at the very beginning of the section on neoclassical theory that it takes into account the toroidal geometry; so all particle motion associated with the curved geometry is considered, specifically, $\nabla B$ and curvature particle drifts[11].

An important prediction of the neoclassical theory is the bootstrap current that we will discuss in the following section.

## 3.3 Bootstrap current

The bootstrap current is a self-generated current which arises in toroidal plasmas driven by temperature and density gradients. Since this current occurs naturally and the tokamak plasma relies on a current for its equilibrium, the bootstrap current can be thought of as an advantage. It is automatically generated if one confines a high-pressure plasma. In principle the bootstrap current can allow for a steady-state tokamak reactor in which only a small fraction of the total current is driven through external means. The relatively low current drive efficiency of the known external non-inductive methods demand a high bootstrap current fraction for the reactor to be economically attractive. What is even more interesting with the bootstrap current, beyond its natural occurrence, is that the steep pressure gradient we have in the plasma edge leads to a large localized bootstrap current, making it the main component of the total plasma current; see figure 3.6. So in a tokamak machine the

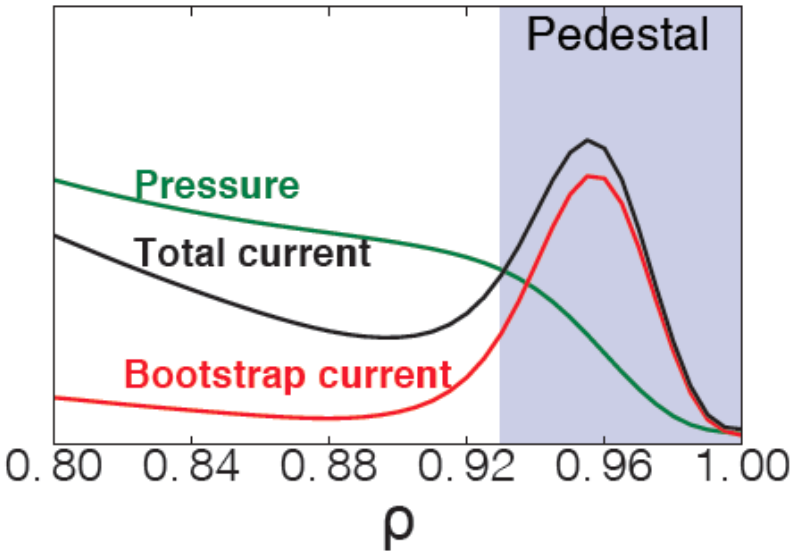


Figure 3.6: Steep pressure gradient in the plasma edge leads to large bootstrap current fraction, almost all the total current in that region

bootstrap current will be typically 70% to 90% of the total current in the edge. The importance of the bootstrap current in confinement, stability and for a steady-state fusion reactor is summarized in the next subsections.

#### Relation between bootstrap current, confinement and MHD stability

There are many studies in literature which focus on bootstrap current implications on stability and confinement. As an example it was found simultaneously by Callen [17] and Carrera [18] that the bootstrap current leads to a type of instability called the neoclassical tearing mode. Basically it can be understood in this way: at a magnetic surface with a rational value of q (the safety factor) even the smallest perturbation in the magnetic field that is resonant with the field line winding changes the topology and generates an island structure. This perturbed magnetic field must be generated by a current of correct helicity and the bootstrap current can supply such a perturbed current. The neoclassical tearing mode is then seen as a clear disadvantage of the bootstrap current. It is expected to be a real issue in a reactor like ITER, possibly leading to an unacceptable degradation of confinement. This is an area of intensive current research.

#### The steady state tokamak reactor

A high fraction of bootstrap current would be necessary for an economically attractive steady-state reactor. This is due to the low efficiency of externally driven current, which is expensive. Following the observation of a high bootstrap current fraction, up to 80% in a JT-60 discharges [19], some reactors have been proposed like the SSTR proposed by M. Kikuchi *et al.* in *Conceptual design of the steady state tokamak reactor (SSTR)*[20] and ARIES-1 devices [21]. The SSTR concept was originally developed in 1989 as a DEMO concept (aiming to demonstrate sustained electric power generation from fusion) see Fig: 3.7. However a reactor with high fraction of bootstrap current would face many issues (from M.Kikuchi work in [24]). Further studies on the feasibility of this reactor and the limitations of a high bootstrap current fraction can be found in [25].

### 3.3.1 The concept of Low and high collisionality

Let's define as $\nu_{ee}$ and $\nu_{ei}$ the electron-electron collision frequencies and the electron-ion frequency. In magnetically confined fusion the collisionality $\nu_*$ is the average number of times a particle is scattered into a passing particle before completing a banana orbit.

$$\nu_* = \frac{\nu R q}{\epsilon^{3/2} v_{th}} \tag{3.17}$$

in Equation 3.17 $\nu$ is the collision frequency $q$ the safety factor $\epsilon$ the inverse aspect ratio, that we will define in more details later, and $v_{th}$ the thermal velocity of the ion or the electrons. The low collisionality regime is when $\nu_* << 1$, in this regime trapped particle exist for many banana regime. This is also called the banana regime. [14][26]. In the other hand when $\nu_* >> 1$ we are in the high collisionality regime,the so called Pfirsch-Schluter regime.

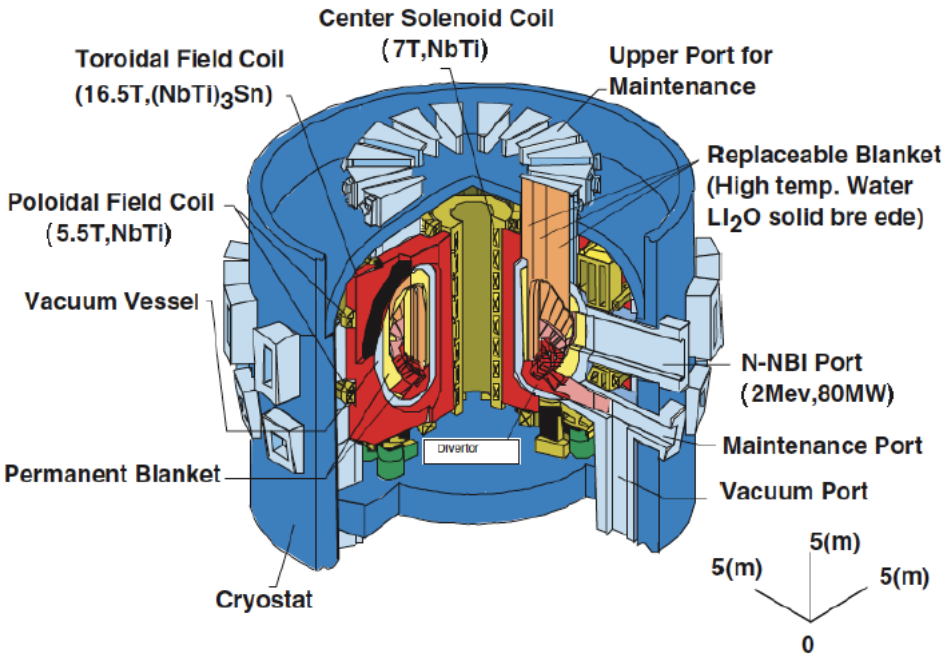


Figure 3.7: View of SSTR(Steady State Tokamak Reactor) tokamak proposed by S.Nishio *et al* in [22][23].

### 3.3.2 The physical mechanism behind the bootstrap current

We mentioned in the previous section that neoclassical transport describes, among other effects, the bootstrap current; especially at in the low collisionality regime. We also pointed out the importance of the boostrap current. The experimental verification of the bootstrap current has been reviewed by Kikuchi and Azumi[27]. The bootstrap current is related directly to the inhomogeneity of the magnetic field strength $B \propto 1/R$. From the conservation of energy ($E = mv^2/2$) and magnetic moment ($\mu = mv^2/2B$) a physical picture of the trapped particle and the related bootstrap current can be given. Let's first focus on an effect called the mirror effect. We can understand mirroring by examining Fig. 3.8. The figure shows the

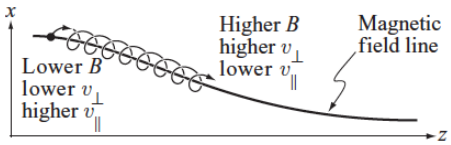


Figure 3.8: The mirror effect: as a particle moves into a region of higher $B$, $v_\perp$ increases and $v_\parallel$ decreases;[11]

trajectory of a particle moving from a region of lower magnetic field to a region of higher magnetic field. The particle starts with a certain value of $v_\perp$ and $v_\parallel$. When the particle reaches the high field region, $B$ increases and as a consequence the perpendicular velocity should increase as well to keep constant the magnetic moment $\mu$. Now let's remember that the total kinetic energy should also remain constant,$E = m(v_\parallel^2 + v_\perp^2)/2$. As a result of this energy conservation an increase of

$v_\perp$ must be accompanied by a decrease of $v_\parallel$. It follows that if the increase in $B$ were very large the particle eventually will reach a point where $v_\parallel = 0$. This point is called the reflection point. Once reflected, the parallel velocity of the particle reverses direction and the guiding center starts moving to the left in Fig. 3.8. With some manipulation one can derive that particles with

$$(\frac{v_\parallel}{v_\perp})^2 < \frac{B_{max} - B_{min}}{B_{min}} \tag{3.18}$$

are trapped in the mirror formed by the magnetic field variation along a field line. $B_{min}$ ($B_{max}$) is the minimum (maximum) magnetic field strength on the magnetic surface. The trapped particles reside on the outboard side and a poloidal projection of a typical orbit is called a banana orbit (see Fig. 3.10). Because of the inhomogeneity of the magnetic field the particles do not follow magnetic field lines exactly but have a drift, which in a tokamak is in the vertical direction, leading to a radial width of the orbit. Let's consider now two trapped ions with the same energy and magnetic moment that start from the same point on the magnetic surface with a different sign of the parallel velocity. From figure 2.8 it can be seen that (with the chosen value of the sign of the poloidal field) the ion with negative (positive) parallel velocity drifts inwards (outwards). The averaged radius of this orbit is smaller (larger) than that of the considered flux surface. Consequently, if a radial gradient in the density exists, this orbit will be populated more (less) than one expects from the density on the flux surface. This leads to an asymmetry in the velocity distribution, also shown in figure 3.9b, with more trapped ions moving in the negative compared with the positive toroidal direction (see Fig. 3.9a). Because the drift of the electrons is in the opposite direction, the asymmetry in the electron distribution has the opposite sign and the radial density gradient leads to a parallel current. This current is how the bootstrap current is generated or at least a part of it that we will refer to as the banana current.The other contribution to the bootstrap current being given by the momentum exchange between the trapped and passing particles.

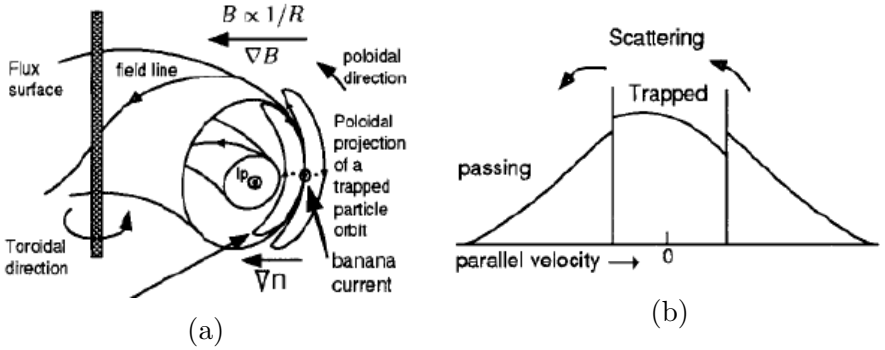


Figure 3.9: (a) More particles follow the orbit further inside than the orbit further out. (b) Distribution function as a function of the parallel velocity for constant perpendicular velocity.[25]

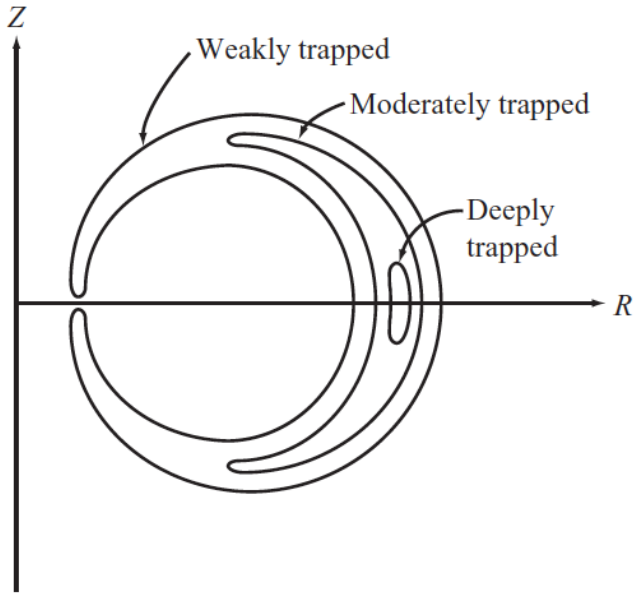


Figure 3.10: Drawing of three banana orbits corresponding to a deeply trapped particle, a moderately trapped particle, and a weakly trapped particle. [11]

# Chapter 4

# Bootstrap current models and their limitations

## 4.1 Definitions

### 4.1.1 The Drift-Kinetic Equation DKE

The "drift-kinetic equation" is the basis for all calculations of neoclassical transport and flows, as well as the bootstrap current. There are several variants of the equation; one standard form is:

$$v_{\|}\vec{b}\cdot\nabla\bar{f}_1 + \vec{v}_d\cdot\nabla f_0 - \frac{Ze}{T}E_{\|}v_{\|}f_0 = C(f_1) \tag{4.1}$$

We already have introduced the maxwell distribution, $f_0$ represent the leading-order maxwellian distribution and $\bar{f}_1$ is the gyroaverated perturbed distribution. We introduced the gyroradius in the previous section, many times plasma quantities are averaged over gyroradii. $\vec{b}$ is the vector along the magnetic field line and most importantly $\vec{v}_d$ is the sum of magnetic, $E\times B$, and parallel drifts we already introduced.

So, the bootstrap current is the self-generated current which arises in our tokamak plasmas driven by density and temperature gradients. Since it is experimentally hard to measure the bootstrap current, we will rely on physics models for the calculation. On the one hand we have first-principle codes like NEO[3] or NCLASS [28] .Those codes, by computing the actual distribution function, can offer a very accurate calculation of the bootstrap current[2]. On the other hand we have analytic models like the well-known Sauter model[5][4] which have the advantages of being fast but are limited in accuracy.In an attempt to improve the accuracy of the Sauter model, another analytic model was developed the: KCK12 model[29] [2], a modification of the Sauter model. The KCK12 failed in trying to improve the Sauter model, and provides a bootstrap current calculation which is not accurate. In the following sections we will present with more details the various bootstrap current models and highlight their limitations.

## 4.2 The first principle code NEO

NEO is a first-principle code that solves the drift-kinetic equation(Equation 4.1) coupled to the Poisson equation. NEO assumes transport to be a local phenomenon, meaning that fluxes at one radial location only depend on plasma parameters at that same radial location.It is important to specify that NEO is part of a suite of codes solving the whole transport equation in a tokamak, NEO solving the neoclassical part and GYRO [30] solving the anomalous(turbulent) part.NEO has been extensively benchmarked with analytic theories, as well as with NCLASS[28] over a wide range of parameters and in various asymptotic limits. (NCLASS is the neoclassical codes that has ben used all over the years for it's excellent accuracy ),

NEO is considered the state-of-the art of neoclassical code, and for our purposes NEO will be used to validate the analytic models, since direct measurement of the bootstrap current is difficult.

## 4.3 The Sauter model

The Sauter model [4, 5] is an analytic formula, developed by Olivier Sauter and Carlo Angioni. The general form of the model is given by:

$$\left\langle j_{\|} B \right\rangle = -I p_e \left[ L_{31} \frac{p}{p_e} \frac{dlnp}{d\Psi} + L_{32} \frac{dlnT_e}{d\Psi} + L_{34} \alpha \left( \frac{p}{p_e} - 1 \right) \frac{dlnTi}{d\Psi} \right] + \sigma \left\langle E_{\|} B \right\rangle \quad (4.2)$$

Where $I$ is related to the toroidal magnetic field strength by $I = RB_{\Phi}$, and $p$ is the total pressure.The coefficients $\sigma$(the neoclassical conductivity), $\alpha$ (the ion parallel flow coefficient) and $L_{31}$, $L_{32}$ and $L_{34}$ are functions of the fitting parameters Sauter has used. These coefficients can be analytically computed from equations (13) through (18) in [4]. the functional form of $j_{\|}$ in equation (4.2) is correctly written in the erratum [5] to the original Sauter et al paper [4]. The erratum also contains the corrected equation for $\alpha$.

The Sauter model then provides a much faster calculation of the bootstrap current than the neoclassical code NEO. It is a fitting formula based on numerous scans with the neoclassical codes CQLP and CQL3D which also solve the drift-kinetic equation (Eq: 4.1) but unfortunately only in the case of pure plasma, which means an ideal plasma constituted only of electrons and main ions (electrons and deuterium ions if considering DIII-D tokamak for example ). Furthermore the Sauter model uses as fitting parameters the trapped fraction (the fraction of trapped particles)the collision frequency, and ion charge. It is clear from those considerations that the Sauter model will be limited in accuracy when applied to realistic plasmas with many impurity species. Another limitation of the Sauter model is that it does not cover all collisionality regimes [2] and typically will underestimate the bootstrap current at low collisionality and overestimate it at high collisionality. We will discuss more in details the accuracy of the Sauter model, now we can mention only that at the time the model was developed, in 1999, Sauter did not have the available resources (computer power etc.) to go to higher collisionalities, while at low collisionalities the inaccuracy comes from the fitting parameters themselves.

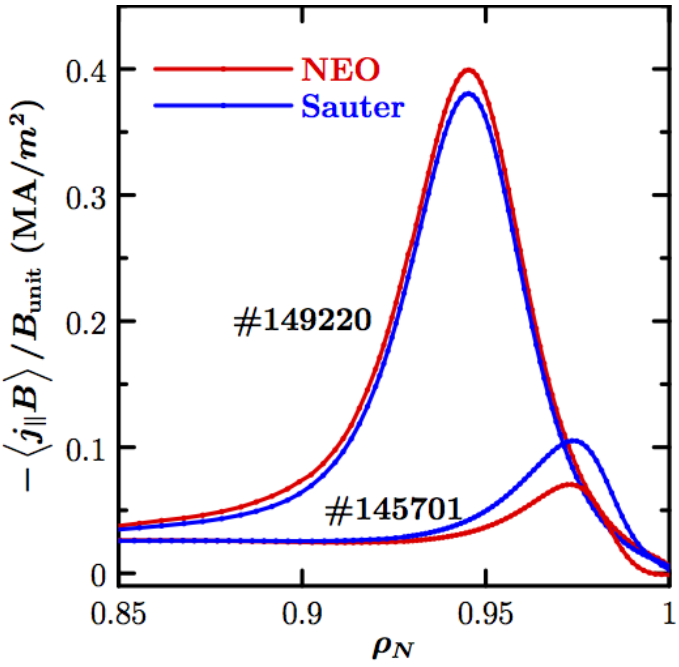


Figure 4.1: NEO vs Sauter bootstrap current. The Sauter model overestimates the current at high collisionality (shot 145701) and underestimates it at low collisionality (shot 149220) . [2]

## 4.4 The KCK12 model

In an attempt to improve the accuracy of the Sauter model, a new model has been proposed by Koh [29]: the KCK12 model. In fact the KCK12 model is not an entirely new formulation; it is rather a modification of the Sauter model. It is based on a fit to simulations with the neoclassical particle code XGC0 [31]. This code still solves a form of the drift-kinetic equation. The objective of the authors was to improve the accuracy of the Sauter model especially in the plasma pedestal and edge. We mention this model in order to illustrate how difficult it can be to improve the accuracy of the Sauter model, during our researc work , while working to make a more accurate formulation, we mainly realized that the model by Sauter was a really good model, many attempts to improve it has failed and it is therefore necessary to work on the details the Sauter model did not consider.

### Comparison of the models

The comparison of the three models was made by E. Belli in [2], considering experimental cases in both the DIII-D and NSTX tokamaks. The entire bootstrap current "radial" profile is analyzed. Let's first discuss the difference between the two tokamaks, which is important for the bootstrap current profiles analysis. The difference in the configuration resides in a parameter called the inverse aspect ratio, $\epsilon$. The aspect ratio $(1/\epsilon)$ is defined as the ration $R/a$; where $R$ $(a)$ is the major (minor) radius. From this definition a tokamak with low aspect ratio (so large $\epsilon$) will be more spherical and a tokamak with low $\epsilon$ are referred to as large aspect ratio tokamak (DIII-D, JET, etc.) (see Fig. 4.2). The aspect ratio is not the only differ-

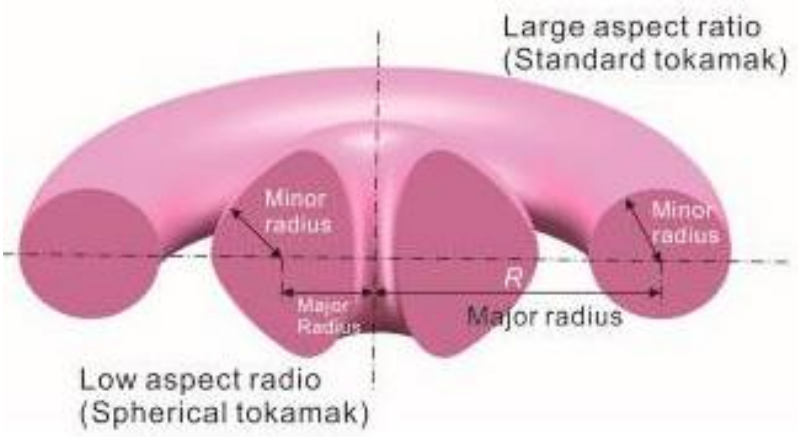


Figure 4.2: Low aspect ratio tokamaks are spherical, an example is the NSTX tokamak; DIII-D is a more starndard tokamak with large aspect ratio. Copyright 2000 America Institute of Physics

ence between the two tokamaks. The temperature in NSTX is generally lower than in DIII-D; this is important since a lower temperature means higher ion collision rate.If we assume for a typical particle $m_e v^2 \approx Te$ it follows that[11]:

$$\nu \approx \frac{n_e e^4}{4\pi\epsilon_0^2 m_e^{1/2} T_e^{3/2}} \tag{4.3}$$

The first comparison we show is in the simplified case of a pure plasma with electrons and only deuterium ions. On DIII-D both the Sauter model and the KCK12 model agree remarkably well with NEO in the pedestal while the relative errors in the core are large. The core is the region of relatively low collisionality, in contrast to the region of high collisionality in the pedestal. The large relative discrepancy observed in the core in Fig. 4.3a is not likely to have a significant effect on the plasma stability since the contribution of the bootstrap current to the total current in this region is small (10-20%). In the NSTX tokamak figure 4.3b shows how the KCK12 model largely overestimates the bootstrap current in the pedestal. This result is sufficient to conclude that the KCK12 model is not an improvement of the Sauter model for NSTX pedestal parameters. E. Belli showed in [2] that the KCK12 model generally is inaccurate for large $\epsilon$ and high collisionality. It appears then at the end of this simplified pure plasma case that the KCK12 model [29], which was designed for large inverse aspect ratio and large collisonality, is probably less accurate than the Sauter model in this regime.

Now let's consider a more realistic case including impurities. We should note that the Sauter model, even if it is often applied to multi-ion plasmas in analysis, is based on fitting coefficients for strictly pure plasmas. Also, because of the lower pedestal temperatures, the regime in the pedestal is essentially a relatively high collisionality regime. The results of this comparison are summarized in Table 4.1.

Table 4.1 shows the clear correlation between the collision frequency and the error. The Sauter model understimates the bootstrap current at relatively low collisionality i.e $\nu_{*e} < 1$ , with increasing error as $\nu_{*e}$ decreases (as we approach the banana regime). Similarly the Sauter model overestimates the bootstrap current for

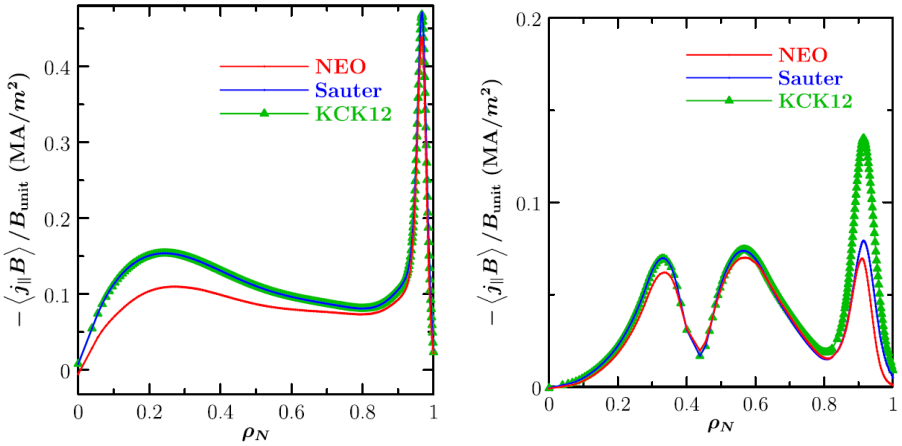


Figure 4.3: Bootstrap current profile comparing the NEO simulation results with the Sauter model and the KCK12 formula, for the case of pure plasma. The error between the NEO result and the respective model is shown for a DIII-D H-mode shot (a), and for an NSTX H-mode (b). [2]

large collisionality $\nu_{*e} > 1$ with error increasing as $\nu_{*e}$ increases towards a regime called the Pfirsch-Schluter regime.

### Impurities

In this section we will discuss the impact of the impurities on the accuracy of the different models. We will compare the Sauter models against NEO simulations for plasma with carbon impurities. We define the carbon impurity fraction as $f_I = Zn_C/ne$. In figure we show a comparison of the NEO results with the Sauter model with varying carbon density scaled uniformly across the profile from the original experimental profile labeled 'exp'.

The effect of impurity species as we move towards the edge is non negligible: this is the reason why the Sauter model that was designed for a pure plasma is not accurate in the pedestal of a multi-ion plasma experiment. The KCK12 model unfortunately was not able to provide a more accurate formula. The NEO code remains the model that provides the most accurate calculation.Being a first-principle code has the consequence of being computationally expensive (especially when we increase the number of species) For a typical bootstrap current profile the NEO code will take about 25 minutes , if we increases the species and the resolution the NEO code can take even an hour to compute a profile. In integrated modelling applications, usually the NEO calculation is embedded into another codes so that the computed bootstrap current is used to study another phenomenon, The fact that the NEO code takes many minutes makes it the slowest part of the modelling and then a crucial issue. Also when we deal with real time analysis, ie analysis taking place while the experiment is being carried out, the NEO calculation is definitely too slow. real time analysis takes very few seconds, and we would need an analytic formula or a formula that only takes seconds or micro-seconds to compute a current profile. These were our motivations to look for a new model to calculate the bootstrap

Table 4.1: Bootstrap current analysis comparing NEO and Sauter for a range of DIII-D discharges. The values of the collision rate $\nu_{*e}$, the carbon impurity fraction $f_I$, the NEO bootstrap current, and the relative error between NEO and Sauter are shown at the radial location of the center of the pedestal.[2]. QH-mode is Quiescent H-mode detailed in [32]

| Shot # | Description | $\nu_{*e}$ | $f_I$ | $\langle j_{boot} \rangle (MAm^{-2})$ | $1 - \frac{\langle j_{boot} \rangle_{sauter}}{\langle j_{boot} \rangle_{neo}}$ (%) |
|---|---|---|---|---|---|
| 149220 | QH-mode | 0.068 | 0.62 | 0.399 | 4.7% |
| 145098 | QH-mode | 0.092 | 0.26 | 0.373 | 2.6% |
| 145421 | H-mode | 0.398 | 0.25 | 0.360 | 1.7% |
| 144987 | H-mode | 1.297 | 0.058 | 0.184 | -20.3% |
| 144977 | H-mode | 1.383 | 0.046 | 0.287 | -18.4% |
| 144981 | H-mode | 2.434 | 0.034 | 0.255 | -32.4% |
| 145701 | H-mode | 4.202 | 0.11 | 0.07 | -49.5% |

current. A model that would be much faster than NEO (at least a thousand time faster) and at the same time more accurate than the analytic Sauter model.

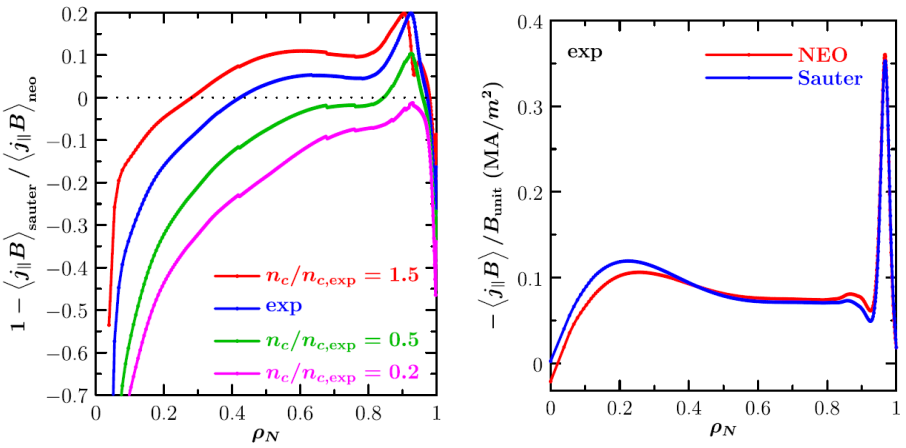


(a) (b)

Figure 4.4: Bootstrap current profile for DIII-D H-mode shot 145421 at t = 2283 ms, comparing the NEO simulation results with the Sauter model 4.4a, for the case of kinetic electrons, deuterium ions, and carbon impurities with varying carbon density scaled uniformly across the profile from the original experimental profile labeled 'exp'4.4b. The fractional error between the NEO result and the respective models is also shown. [2]

# Chapter 5

# Neural network approach

The Neural Network paradigm is capable of breaking the speed-accuracy trade-off that is expected in traditional physics models. In the field of magnetic fusion it already has been applied to many other problems. As an example, it has been used to predict the onset of plasma disruptions [33, 34] and real time control systems [34]. More recently it also has been successfully used to predict turbulent transport fluxes and the pedestal structure [7]. The model for the prediction of turbulent fluxes and pedestal structure was developed at General Atomics, in the same group where this thesis work has been done. Our motivation was to try and apply the Neural Network approach to predict experimental bootstrap current profiles. Let's

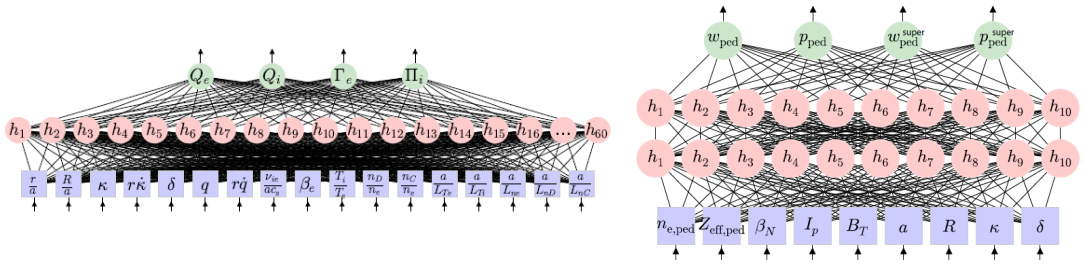

(a) (b)

Figure 5.1: Neural Network based models used to predict turbulent transport fluxes 5.1a, and the pedestal structure 5.1b. [7]

go back first over the very basic principle of Neural Networks.

## 5.1 Neural Networks (NN) generalities

Neural Networks, either artificial or biological, are vast networks of neurons. The artificial neural network was inspired by the complex biological network of neurons in the human brain. The natural neuron receives signals through synapses located on the dendrites or membrane of the neuron. The single natural neuron then, when it receives signals that surpass a certain threshold, is activated and emits a signal through the axon. This signal can be propagated to other neurons and so forth.

To study Artificial Neural Networks it is good to start from the single neuron. First because many neural network models are built out of single neurons. And

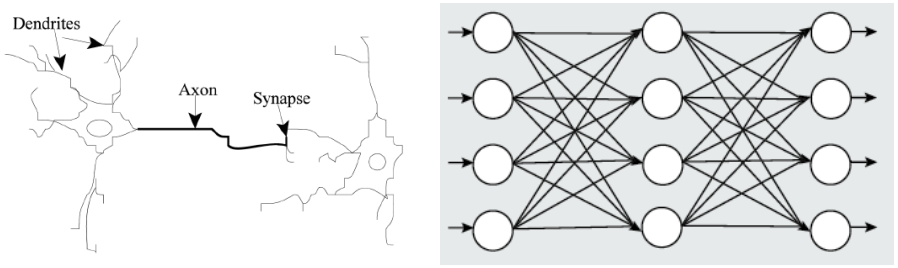


(a) (b)

Figure 5.2: Biological Neural network (in the human brain ) 5.2a. Artificial neural network: artificial neurons are organized in layers with connections. 5.2b.

second because a single neuron is itself capable of "learning". Before we proceed let's clarify the difference between supervised neural networks and unsupervised neural networks. Supervised neural networks are given data in the form of inputs and targets, the targets being the teacher's specification of what the neural network's response should be. Unsupervised neural networks are given data in an undivided form – simply a set of examples – where the algorithm should find the patterns. We focus on supervised neural networks.

**The single neuron**

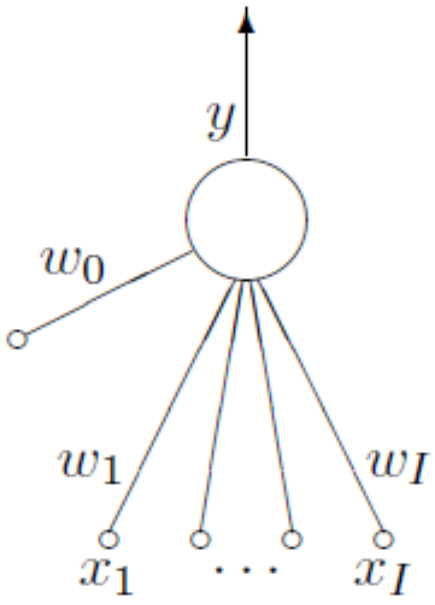


Figure 5.3: A single neuron [35].

A single neuron illustrated in figure 5.3, has a number of inputs $x_i$ and one output that we will here call $y$. Each input is associated with a weight $w_i$. Sometimes there is a parameter $w_o$ called the bias. The connections of the single neuron are directed

from its inputs to its output: it is a feedforward device. When the single neuron receives inputs its activation is computed as $a = \sum_i w_i x_i$.The output of the single neuron is then set as a function $f(a)$ of the activation; $f$ is generally a sigmoid function. If the single neuron is in a network with other neurons, the output $f(a)$ is fed to the neurons of the next layer.

For a network, several configurations and architectures exist. We focus on the one that is generally called Multi-Layer-Perceptron (MLP). It consists of an input layer with $n_O$ entries, one or more intermediary layers and one output layer with $n_m$ outputs. Neurons of each layer are connected with all the neurons of the previous layer. The weights are determined with the aid of the set of known input-output pairings, called the training set. An error function related to the differences between these expected values and the ones delivered by the network is then minimized by iteratively modifying the weights. Each time the weights are modified corresponds to one iteration or one epoch. The mean squared error is generally chosen for the iterative minimization, which is a standard and efficient method.

## 5.2 Neural network for the bootstrap current

In this section we will explain how we used Neural Networks to predict the bootstrap current. We will also define all the important quantities we used for the fitting.

From the flow equations the neoclassical bootstrap current can be defined as

$$\left\langle j_\parallel B \right\rangle = \sum_a z_a e \left\langle n_a u_{\parallel,a} B \right\rangle \ , \tag{5.1}$$

where the subscript $a$ denotes the species index, $z_a$ the charge of the specie $a$ and the angle brackets denote a flux-surface average (we already introduced the flux-surface). The species-dependent parallel flow is given by

$$u_{\parallel,a} = \frac{1}{n_a} \int d^3v v_\parallel f_{1a} \ , \tag{5.2}$$

where $f_{1a}$ is the first-order distribution function for species $a$ which can be computed via solution of the drift-kinetic equation [26]. The source term in the drift-kinetic equation is given by

$$\mathbf{v}_D \cdot \nabla f_{0a} = -\frac{df_{0a}}{dr} \left( v_\parallel^2 + \mu B \right) \left( \frac{I}{\psi'} \frac{\mathbf{b} \cdot \nabla B}{\Omega_{ca} B} \right) \ , \tag{5.3}$$

where $f_{0a}$ is the zeroth-order equilibrium distribution function, which has the Maxwellian form

$$f_{0a} = \frac{n_a}{(2\pi v_{ta}^2)^{3/2}} e^{-v^2/(2v_{ta}^2)} \ , \tag{5.4}$$

$v_{ta} = \sqrt{T_a/m_a}$ is the thermal speed, $\Omega_{ca} = z_a eB/(m_a c)$ is the gyrofrequency, $\psi$ is the poloidal flux divided by $2\pi$, $\psi' = \partial\psi/\partial r$, and $I(\psi)$ is related to the toroidal magnetic field stregth by $I(\psi) = RB_t$. Note that

$$\frac{df_{0a}}{dr} = f_{0a} \left[ \frac{d \ln n_a}{dr} + \frac{d \ln T_a}{dr} \left( \frac{v^2}{2v_{ta}^2} - \frac{3}{2} \right) \right] \ . \tag{5.5}$$

Because the drift-kinetic equation is a linear PDE(Equation 4.1)[14][36] and the neoclassical source term is linear in the equilibrium gradients, the distribution function itself and thus the bootstrap current can be separated into a sum of coefficients multiplied by the equilibrium gradients for each species, as follows:

$$\langle j_{\|} B \rangle \sim \sum_a C_{na} \frac{d \ln n_a}{dr} + C_{Ta} \frac{d \ln T_a}{dr} \ . \tag{5.6}$$

We find it convenient to normalize the coefficients as follows:

$$\frac{\langle j_{\|} B \rangle}{j_{\rm GB} B_{\rm unit}} = -\frac{I}{\psi'} a \sum_a |z_a| \frac{n_a}{n_e} \left[ C_{na} \frac{d \ln n_a}{dr} + C_{Ta} \frac{d \ln T_a}{dr} \right] \ , \tag{5.7}$$

where we have separated out the flux-function geometry factor $I/\psi'$ in the neoclassical source term in equation (5.3). In equation (5.7), we have introduced the normalizing gyroBohm unit of current

$$j_{\rm GB} = e n_e c_s (\rho_{s,\rm unit}/a) \ , \tag{5.8}$$

where $c_s = \sqrt{T_e/m_D}$ is the deuteron sound speed, $T_e$ is the electron temperature, $n_e$ is the electron density, $m_D$ is the deuteron mass, and $\rho_{s,\rm unit}$ is the effective ion-sound gyroradius,

$$\rho_{s,\rm unit} \doteq \frac{c_s}{e B_{\rm unit}/(m_D c)} \ . \tag{5.9}$$

Here the effective magnetic field $B_{\rm unit}$ is defined with reference to a global equilibrium through the relation $B_{\rm unit}(r) = (q/r)\psi'$. Besides the complicated mathematical expressions which arises mainly from normalization and geometric coefficients, the important thing to remember is that the bootstrap current can be written as a sum over all the plasma species of the drivers (density and temperature gradients) multiplied by coefficients. Those coefficients $C_{na}$ and $C_{Ta}$ can be computed directly from the numerical solution of the drift-kinetic equation. As an alternative, we can train a Neural network to perform a nonlinear multivariate regression of each coefficient as a function of selected local dimensionless parameters. We built the network using the state-of-the art integrated modelling tool OMFIT (One Modeling Framework for Integrated task) [37]. OMFIT provides a platform to build the network and compiles databases on which we can train it and benchmark its performance.

## 5.3 Some useful definitions in the framework of Neural Networks

**libraries**

In computer science a library is a collection of resources used by computer programs. These may include configuration data, documentation, pre-written codes and subroutines, classes etc.In the field of Neural networks there are many open source libraries and usually we will rely on those to build neural network models for our purposes.

#### Training data set

The dataset which is the ensemble of data available for the model are a set of inputs and outputs. Each output corresponds to an input. Usually the dataset is divided ion two parts, the training dataset and the validation dataset. The training dataset the part of the total datasey used during the training of the NN. Each programmer is free to divide the dataset as he desires, usually more data are chosen for the training than for the validation.

#### Over-training, Over-fitting

A neural network is said to be over-trained, when the training has led to a situation in which the NN is not able to generalize anymore. This means that the NN has been trained too much to reproduce the data on the traning dataset, and is not able to extrapolate to data it has never seen during the training. Figure 5.4 illustrates how a dataset is being over-trained,the fitting that should be a line is a curve trying to reproduce any single point of the training dataset including noises.

#### learning and learning rate

The learning process is a process during which the NN adjusts the weights of the connections. The NN reads an input , try to predict the output and change the weights according to the difference between the predicted output and the desired output. This process has been described in the previous section. The learning rate instead can be defined as the capabilty the NN has to abandon old belief to a new one.In scientific terms the learning rate is a hyper-parameter that controls how much we are adjusting the weights of our network with respect the loss gradient. It may need few iterations to find the adequate number for each network.

#### weight decay, connection weight

When training neural networks, it is common to use weight decay where after each update, the weights are multiplied by a factor slightly less than 1. This prevents the weights from growing too large.

## 5.4 Algorithm

We used the FANN (Fast Artificial Neural Network) library to build our network. We split all the dataset into a training dataset and a validation dataset. The training dataset is used to adjust the weights on the neural network, while the validation dataset is used to ensure that the model is not over-trained. One has to be careful about over-training, because an over-trained NN will be good on the training dataset and will lose its capability to extrapolate on new data. In this work, an ensemble of 16 neural networks was developed, each with 3 hidden layers of 10 neurons each. Each network is fully connected. The learning rate was set to 0.7 and the weight decay was set to 0.1. The neural networks in the ensemble use the same training and validation datasets but are initialized with random connection weights. A single prediction is given using an average of the outcomes from the ensemble of neural

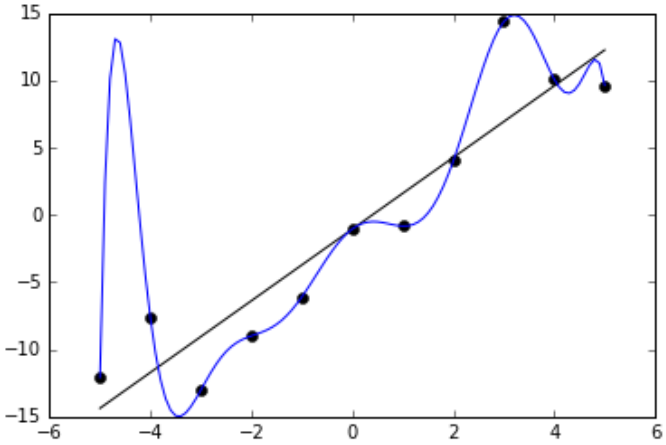


Figure 5.4: An illustration of Over-training.

networks. Using an ensemble, rather than a single neural network, helps to obtain a reliable estimate of the error.

## 5.5 Parametrization

The training dataset is obtained from a large database of runs with the NEO code [3, 38], which provides a direct solution of the drift-kinetic equation. We used more than 57000 NEO runs; this was to ensure that we were covering ranges of parameters relevant for a typical large aspect ratio tokamak (See Table 5.1). Also, we wanted to cover the high collisionality regime, which was lacking in the Sauter model. We considered to begin a three species plasma consisting of electrons, deuterium ions, and impurity ions. The plasma densities are assumed to be quasi-neutral, and the ion species are assumed to be in thermal equilibrium with equal temperatures. Six input parameters are chosen, describing the geometry, collisionality, and ion-impurity physics:

| | |
|---|---|
| $\epsilon$ | inverse aspect ratio |
| $f_t$ | trapped fraction |
| $q$ | safety factor |
| $\bar{\nu}_e$ | electron collision rate |
| $n_i/n_e$ | main ion-to-electron density ratio |
| $T_i/n_e$ | ion-to-electron temperature ratio |

Here $\epsilon$=$r/R_0(r)$, where $r$ is the midplane minor radius $R_0$ is the major radius of the flux surface, and the effective fraction of trapped particles is defined as

$$f_t = 1 - \frac{3}{4}\left\langle B^2 \right\rangle \int_0^{1/B_{\max}} \frac{\lambda\, d\lambda}{\left\langle \sqrt{1-\lambda B} \right\rangle}\,, \tag{5.10}$$

where $\lambda = v_\perp^2/(v^2 B)$ is the pitch angle parameter. For general geometry, it is assumed that the geometry equilibrium data is captured entirely by $\epsilon$, $f_t$, $q$, and the $I/\psi'$ overall scaling factor in equation (5.7). For the collision frequency parameter,

| Parameter | min value | max value |
|---|---|---|
| $\epsilon$ | 0.05 | 0.35 |
| $f_t$ | 0.323 | 0.766 |
| $q$ | 1 | 10 |
| $\bar{\nu}_e$ | 0.01 | 10 |
| $ni/ne$ | 0.6 | 0.99 |
| $Ti/Te$ | 1.0 | 3.0 |

Table 5.1: Range of the fitting parameters

we introduce the dimensionless electron collision frequency [2],

$$\bar{\nu}_e = \frac{R_0}{c_s}\tau_{ee}^{-1} = \frac{R_0}{c_s}\frac{\sqrt{2}\pi e^4 n_e}{m_e^{1/2}T_e^{3/2}}\ln\Lambda\ . \tag{5.11}$$

The dimensionless effective electron collision frequency is related to this by

$$\nu_{*e} = \frac{4}{3\sqrt{\pi}}\frac{q}{\epsilon^{3/2}}\frac{n_i c_s}{n_e v_{te}}Z_{\text{eff}}\bar{\nu}_e\ , \tag{5.12}$$

where $Z_{\text{eff}}$ is the effective charge, which for the case of a single impurity species is $Z_{\text{eff}} = (n_i + Z_I^2 n_I)/n_e$.

## 5.6 Training

The training dataset is obtained from running the NEO code. We assumed that the geometry equilibrium data is captured entirely by $\epsilon$, $f_t$, and the $I/\psi'$ scaling factor. Note that the trapped fraction is not a direct input for NEO, but is rather an intermediate parameter dependent on $\epsilon$ and the assumed geometry equilibrium model. It is well-known that the trapped fraction is the appropriate parameter describing the geometry in banana-regime neoclassical transport theory [14]. In the Pfirsch-Schluter regime, the geometry dependence is weaker [36]. Here we consider as the impurity species fully stripped carbon ions with $z_I$=6, though the model can easily be retrained for different impurity ion species. The input values are as follows:

Usually with a normal resolution, a bootstrap current profile has about 250 points. We have to run NEO once to get a set of input-output for each of our 6 coefficients, this means that we need to run NEO six times to get the set of input-outputs for the 6 coefficients at one radial location.To cover a typical profile we would need $6 \times 250 = 1500$ NEO runs. So to train the NN on 38 discharges for example $38 \times 1500 = 57000$ NEO runs are needed. All these NEO runs were made easy by the fact that NEO can be run in parallel , furthermore NEO is also considered to be a very fast code among other neoclassical codes, If we used heavier codes like NCLASS or XCG0 we could not get all those data points in a reasonable time.

In Figure 5.5 it is represented the Neural Network we built to predict our coefficients. First of all it is important to remember that we have assumed the transport to be a local phenomenon, meaning that the outputs (fluxes, transport coefficients, etc.) at one radial location only depend on plasma parameters at that same radial location. This assumption is reflected in the topology of the NN (see Fig. 5.5), which has

only one neuron for each of the input/output quantities. This should be contrasted to a global transport assumption, which would require multiple neurons for each input/output quantity for the NN to have knowledge of the plasma parameters at multiple locations across the plasma radius. In general, this assumption is satisfied by turbulent and neoclassical transport phenomena at sufficiently small Larmor radii.The NN approach we describe in this work does not make any simplifying assumption about the functional form of the underlying transport physics, besides locality. Always looking in figure 5.5 we can observe 3 hidden layers(layers in between the input and the outputs layers ). Figure 5.6 is a very important figure, it shows

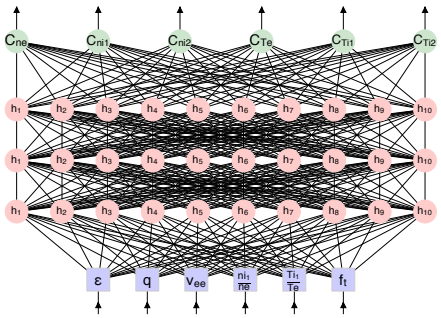


Figure 5.5: A representation of the Neural Network we have built to predict the coefficients for the bootstrap current. The configuration has allowed an accuracy within 1%.

how smooth the parameters are over a long range of collisionality. The fact that the coefficients are smooth tells us that their prediction with NN can be done with high accuracy. The idea of developing this new formula with these coefficients as unknowns is a good one, since a functional form of the coefficients can be given in a future work.

A proof of the fact that the NN will perfom well in predicting our coefficients is shown in Figure 5.7. Where the training error and the validation error are shown, the both decrease with the number of epoch (we defined an epoch in the beginning of the chapter). The data for the training both cover the same dataset the only difference is that we trained on 3/4 of the dataset and we validated on the remaining 1/4 of the data.

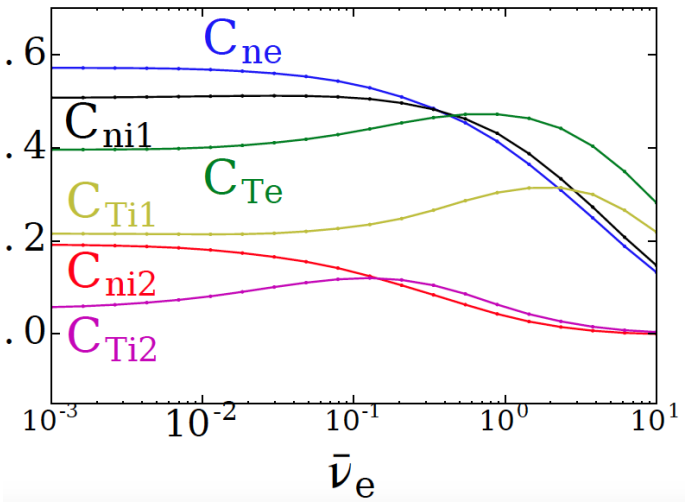


Figure 5.6: The coefficients $C_{Ta}$ and $C_{na}$ are smooth over range of collisionality. this is the reason why the neural network successfully predicted them. The new formulation of the bootstrap current as the sum of theses coefficients was the best approach to develop a NN model to predict bootstrap current profiles.

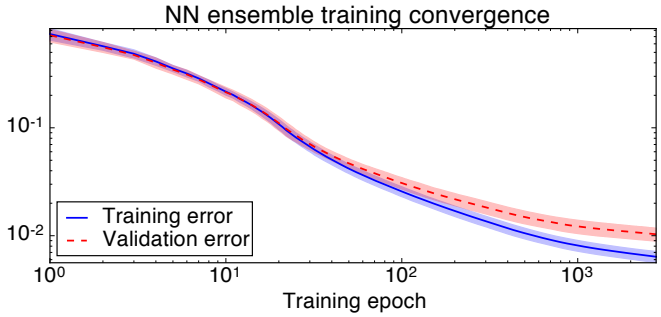


Figure 5.7: Training and validation errors. The validation error going down as fast as the training error is the proof that we did not over-trained the network. It still will be good even in data it never saw during the training.

# Chapter 6

# Accuracy of the NN model

It is now time to discuss the accuracy of our model. Here we intend to discuss the accuracy of our actual physics model. This do not include only the capability of the NN to predict the coefficients, but also how good are the selected input parameters to capture the underlying physics. The most important part of our entire work was the understanding of the parameters we will use to accurately predict the coefficients. If we trained the NN with other input parameters, the NN would still be predicting the six coefficients as a function of those parameters, but this would not mean the NN is giving the coefficient that will produce the correct bootstrap current profile.The goal of this chapter is to compare and discuss the accuracy ofour coefficients against the NEO and Sauter coeffcients. It is important to remember that the two targets for our model were quickness and accuracy.The NN model is as fast almost as an analytic formula requiring only a few $CPU - \mu s$ per data point, what we need now is to evaluate how accurate it can be. To evaluate the accuracy of the model, we consider a representative DIII-D H-mode discharge at the location in the pedestal where the bootstrap current is maximum. DIII-D H-mode shot #145421 has previously been extensively analyzed for bootstrap current physics in reference [2]. An important parameter to define first is the radial coordinate $\rho$. $\rho$ tells us at which location we are , in the radial dimension, $rho \approx 0$ will indicate the core of the plasma and $rho \approx 1$ the edge of the plasma. For simplicity for our purposes we can define $\rho$ as : $\rho = r/a$, r is the radius we are considering and a is the plasma minor radius, $\rho$ is a dimensionless parameter then. Many other plasma geometrical parameters as the plasma elevation $Z_0$,the plasma elongation $\kappa$ the triangularity $\delta$ and the squareness $\zeta$ are well defined and explained in [39].

The NEO-computed bootstrap current was found to be maximum at $\rho$=0.968 with a value of 0.360 MA/m$^2$. The equilibrium and geometry parameters at this location are listed in table 6.1.

For these parameters, a scan of the bootstrap current density and temperature gradient scaling coefficients $C_{na}$ and $C_{Ta}$ over electron collision rate $\bar{\nu}_e$ is shown in Figure 6.1. The Sauter model and neural network model are compared with the NEO simulation results. For circular plasma parameters (same as training data), the inaccuracy of the neural network is less than 3%. Figure 6.2 shows the difference in the variation of the trapped fraction with $\epsilon$ between a circular and the shaped plasma. The dominant geometry influence results from the large triangularity and triangularity gradient. For the shaped plasma, the neural network shows better qualitative agreement with NEO than the Sauter model for each of the coefficients

Table 6.1: Equilibrium and geometry parameters for DIII-D #145421 at the location in the pedestal where the bootstrap current is maximum. Here $R_0$ is the major radius, $Z_0$ is the elevation, $\kappa$ is the elongation with $s_\kappa = (r/\kappa)d\kappa/dr$, $\delta$ is the triangularity with $s_\delta = rd\delta/dr$, $\zeta$ is the squareness with $s_\zeta = rd\zeta/dr$.

| | | | |
|---|---|---|---|
| $\epsilon$ | 0.339 | $dR_0/dr$ | -0.269 |
| $q$ | 4.435 | $Z_0$ | -0.029 |
| $\bar{\nu}_e$ | 0.798 | $dZ_0/dr$ | -0.886 |
| $n_i/n_e$ | 0.741 | $\kappa$ | 1.775 |
| $z_I$ | 6 | $s_\kappa$ | 1.558 |
| $m_I/m_i$ | 6 | $\delta$ | 0.407 |
| $n_i/n_e$ | 0.043 | $s_\delta$ | 1.955 |
| $T_i/T_e$ | 1.564 | $\zeta$ | -0.042 |
| | | $s_\zeta$ | -0.228 |

at high collision frequency, $\bar{\nu}_e > 1$. The inaccuracy of the Sauter model at high collision frequency has been reported previously [40, 2]. More significantly, the neural network provides a large improvement for the impurity coefficients, for which the Sauter model does not accurately reproduce the trend with collisionality. Although the Sauter model is often applied to multi-ion plasmas, it is based on fitting coefficients for cases of strictly pure plasmas. It was previously found that the Sauter model is able to accurately capture the electron-impurity interaction through the use of $z_{\text{eff}}$ in $\nu_{*e}$ due to the large mass ratio separation between the two species, but does not accurately model the ion-impurity interaction [2]. While the contributions of the impurity density and temperature gradient scaling coefficients to the bootstrap current are generally small due to the small carbon impurity fraction, they can become important in the plasma edge.

### A more detailed comparison of the models

Figure 6.3 shows the trend of the coefficients $C_{ne}$ and $C_{Te}$ with increasing collision frequency. In principle the Sauter model and the NN model should be following the red curve of the NEO model.The Sauter model,designed for pure plasmas should be able to capture at least the electron physics. This is what happens at low collisionality where the three curves are very close for both the temperature and the density coefficient. Discrepancies arise when we move from low to high collisionality regime. Here while the NN model still follows the trend of the NEO model, the Sauter model is unable to reproduce the same result. These plots show how, at least for the electron physics, the NN is doing a better job especially at high collisionality. The good performance of the NN is due to our training dataset that we purposely extended to very high collisionalities, which was made easy by the quickness of the NEO code: we could run it in parallel very quickly and increase our data ranges. This feature is not possible with other neoclassical codes like NCLASS.

Figure 6.4 instead focuses on the main ion physics. The coefficient for the ion density gradient is well captured by the Sauter model and the NN model . For the temperature gradient, while the NN follows the trend of the NEO coefficient, the Sauter model exhibits a strange behaviour. This trend is due to an error in the

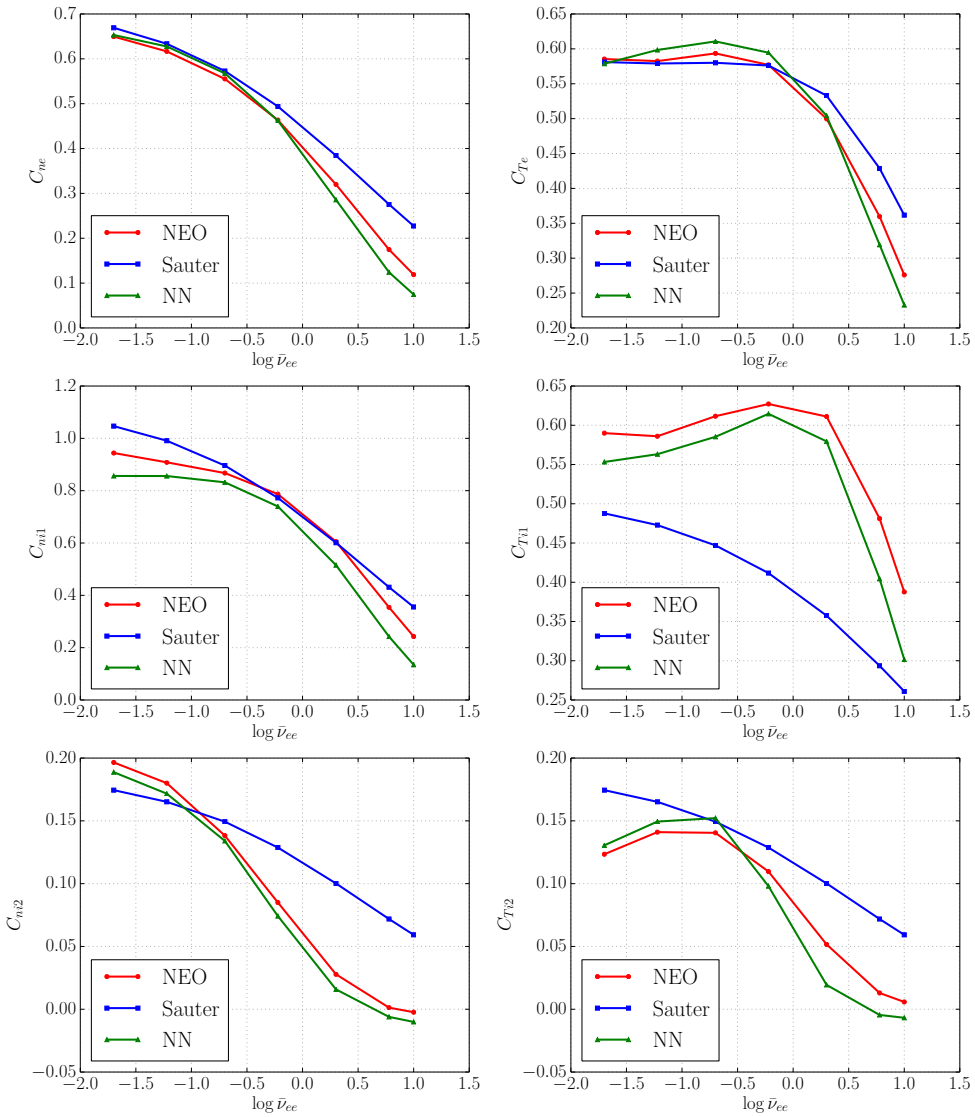


Figure 6.1: Bootstrap current density and temperature gradient scaling coefficients versus electron collision rate for the DIII-D-like pedestal parameters given by table 6.1, comparing NEO simulation results with the Sauter model and the neural network model.

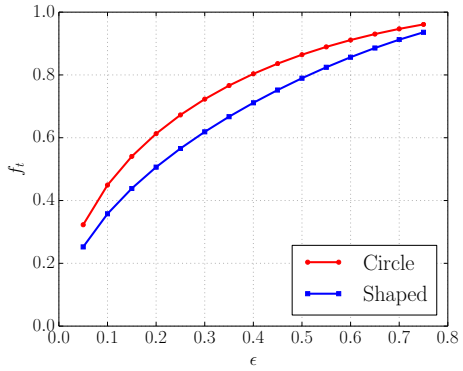


Figure 6.2: Trapped fraction versus inverse apsect ratio comparing a circular plasma with a shaped plasma using the DIII-D-like pedestal geometry parameters in table 6.1.

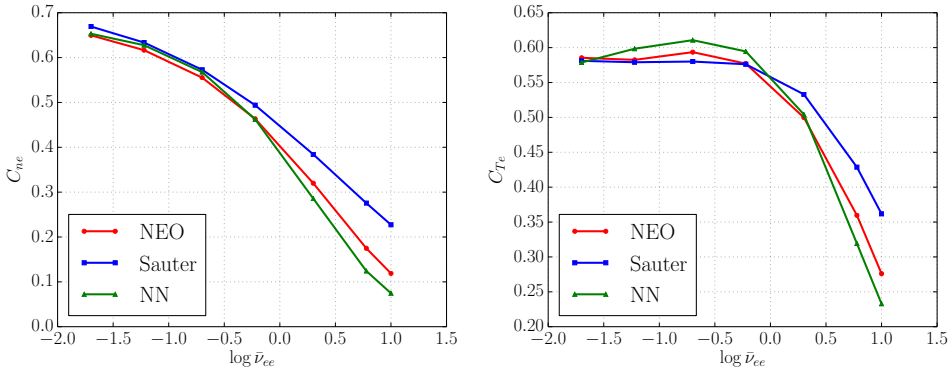


Figure 6.3: Electron temperature and density gradient coefficients compared

analytic formulation of the Sauter model, the error is pointed out in [2].

The pair of coefficients in Figure 6.5 are the ones showing how the different models capture the impurity physics. We have already mentioned that the Sauter model was meant for pure plasmas, so without any surprise the Sauter model does not reproduce the trend of the coefficients independently of the collision frequency we choose. On the other hand the NN model performs a great job, by closely following the NEO model. This pair of plots clearly shows that the NN model is much more accurate than the Sauter model by the fact that it captures very well the impurity physics.

### Conclusion on the accuracy

It is important to conclude this section by highlighting the fact that the improvement in accuracy of the NN model over the Sauter model comes mainly from two sides.The fact that we explored higher collisionalities regime , and the inclusion of the impurities. We carefully selected the fitting parameters so that even at lower collisionalities we still have good results. The NN did not introduce itself any physics or any assumption; it has been helpful to quickly calculate the coefficients we needed for our model (actually a physics model). We preferred this fitting method (Neural Network non linear regression) because it is accurate and quick. It was perfectly combined with our analytic theory to provides a model which is as fast as a pure analytic one and at the same time very accurate. By Analytic theory we mean the

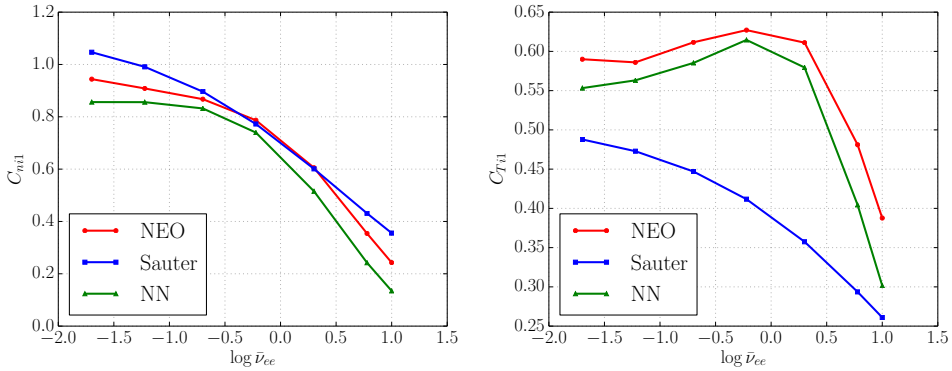


Figure 6.4: Main ion temperature and density gradient coefficients compared

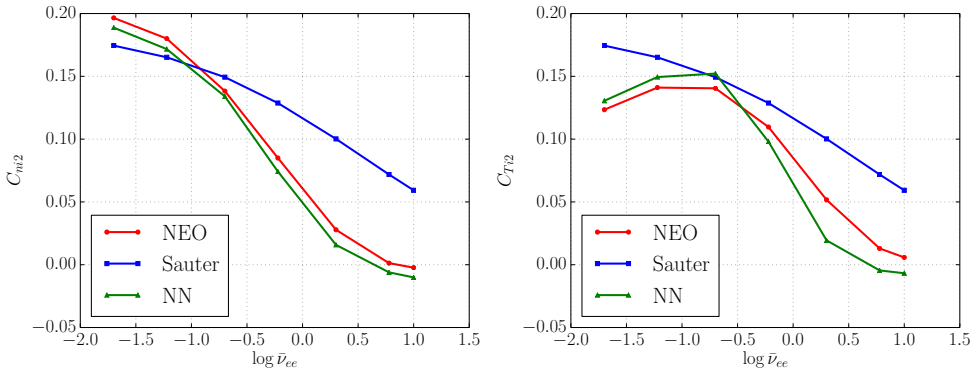


Figure 6.5: Impurity temperature and density gradient coefficients compared

fact that we have re-written the bootstrap current as in the Equation 5.7. In this way we used the NN to predict only the coefficient for the temperature and density gradients $C_{Ta}$ and $C_{na}$. The series of figures we showed in this Chapter show the accuracy of our model.

# Chapter 7

# NN prediction of experimental bootstrap current profiles

## 7.1 DIII-D

In this section, we explore the accuracy of the prediction of the bootstrap current profile from the neural network model compared with the NEO solution for representative DIII-D QH-mode and H-mode plasmas covering a range of collision regimes and carbon impurity fractions. The results for the fractional discrepancy between NEO and the Sauter and neural network models are shown in table 7.1. For each case, the neural network shows better agreement than the Sauter model in both the core and the edge. The improvement is particularly notable for higher collisionality cases. Profiles of the edge bootstrap current for the moderate collisionality and high collisionality DIII-D cases are shown in figure 7.1 and figure 7.2. Similar results were found for JET, as shown in table 7.2.

### A closer look at low collisionality

Figure 7.4 shows a bootstrap current profile in a case of low collisionality in DIII-D. It appears that both the Sauter model and our NN model are doing great. This case is interesting because even in this case where the Sauter model was showing

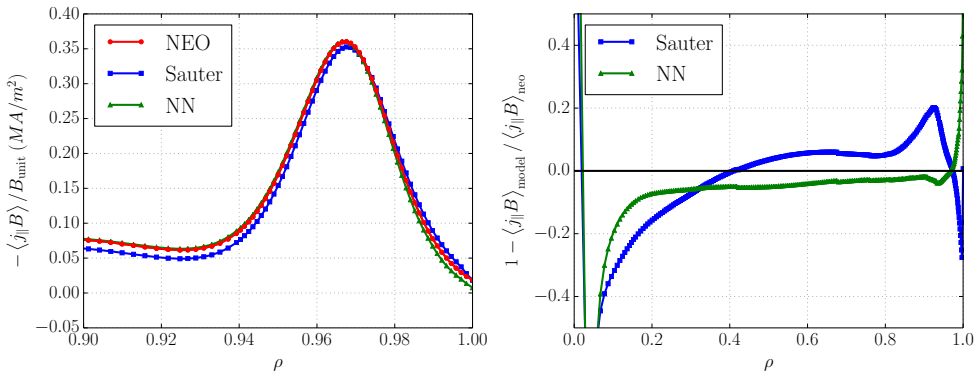


Figure 7.1: Bootstrap current edge profile for DIII-D H-mode shot #145421 at t=2283 ms, comparing NEO simulation results with the Sauter model and the neural network model. The fractional error between the NEO results and the respective models is also shown for the entire profile.

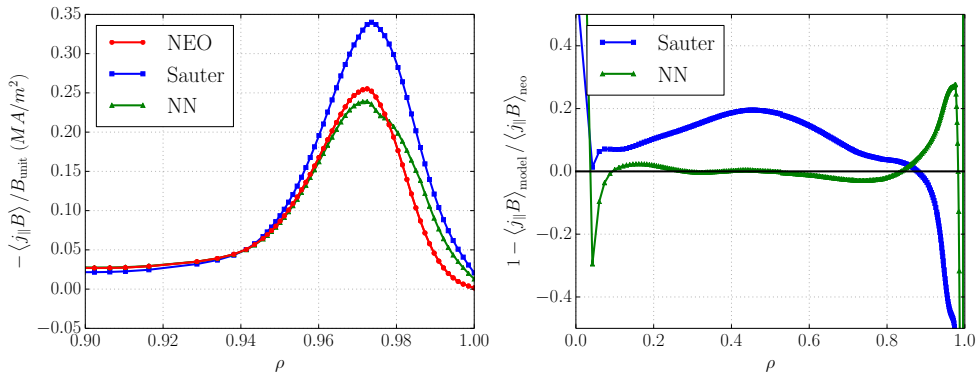


Figure 7.2: Bootstrap current edge profile for DIII-D H-mode shot #145701 at t=59 ms, comparing NEO simulation results with the Sauter model and the neural network model. The fractional error between the NEO results and the respective models is also shown for the entire profile.

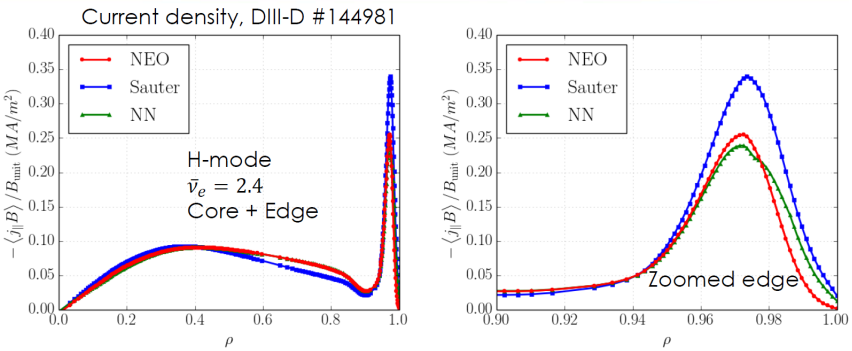


Figure 7.3: Shot #145701 zoomed the main discrepancies arise in the edge.

Table 7.1: Bootstrap current model analysis comparing NEO simulation results with the Sauter model and the neural network model for a range of DIII-D QH-mode and H-mode discharges. The values of the effective electron collision rate $\nu_{*e}$ and the carbon impurity fraction $f_I = z_I n_I / n_e$ are shown at the radial location of the center of the pedestal. The values for the Sauter model and the neural network model are the mean values in the core ($0 \leq \rho < 0.9$) and in the pedestal ($0.9 \leq \rho < 0.99$) of the percent error between the NEO result and the model, $100(1 - \langle j_\parallel B\rangle_{\rm model}/\langle j_\parallel B\rangle_{\rm neo})$.

| DIII-D Shot # | $\nu_{*e}^{\rm ped}$ | $f_I^{\rm ped}$ | Core Sauter | Core NN | Edge Sauter | Edge NN |
|---|---|---|---|---|---|---|
| 149220 | 0.068 | 0.623 | 8.0% | 1.5% | 7.7% | 7.3% |
| 145098 | 0.092 | 0.262 | 10.2% | 2.3% | 4.7% | 3.2% |
| 145421 | 0.378 | 0.259 | 7.5% | 4.9% | 9.6% | 3.4% |
| 144987 | 1.297 | 0.058 | 7.0% | 2.8% | 29.9% | 14.0% |
| 144977 | 1.383 | 0.046 | 7.5% | 0.9% | 19.2% | 6.8% |
| 144981 | 2.434 | 0.034 | 9.2% | 1.0% | 34.2% | 11.7% |
| 145701 | 4.202 | 0.108 | 11.4% | 1.4% | 38.9% | 21.0% |

particularly accurate results, we still were able to provide a more accurate result. Not only we improved the model at high collisionality, but even at low collisionality we can offer a more accurate bootstrap current.

We discussed why the Sauter model behaves poorly at high collisionality; here we will offer the physical reason why at low collisionality we can offer a more accurate result. The low collisionality regime is also called the "Banana regime". The three parameters Sauter used for the fitting of the coefficients for the bootstrap current are : $\nu_{*e}$, $f_t$, $Z_e$. The limitation at low collisionality comes from the parameter $\nu_{*e}$ which in the banana regime cannot be considered a single parameter; in fact it should be separated in those three parameters: $q$, $\epsilon$, $\nu_e$, and each variation of those parameters should be considered a part. This is because $\nu_{*e} \sim \frac{q}{\epsilon^{3/2}} \frac{\tau_e e^{-1}}{c_s/R_0} \frac{n_i}{n_e}$ [2]. This shows how we also improved at low collisionality: we selected separately as our 3 input parameters ($q$, $\epsilon$, $\nu_e$) rather than encapsulate them inside the $\nu_{*e}$ .

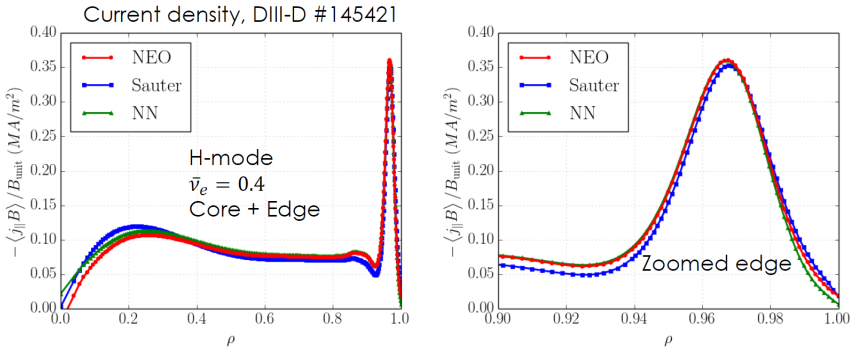


Figure 7.4: Sauter and NN botstrap current compared at low collsionionality. With the zoom into the edge it is clear that both models behave well. Still the error associated with the NN is smaller. Sauter: 9.6% error; NN: 3.4% error.

## 7.2 JET

We applied the new method to the JET tokamak and similar results have been obtained as indicated in table 7.2.

## 7.3 ITER and the future tokamak reactors

To conclude our discussion let's discuss how the new bootstrap current calculation will behave when it will be applied to the ITER tokamak.

### ITER

ITER which means *"the way"* in Latin is certainly one of the most ambitious engineering and physics projects today. It is a magnetic fusion device which is being constructed in southern France. The project is funded and run by by 7 members entities: the European Union, India, Japan, China, Russia, South Korea, and the United States. The main goal of ITER is to demonstrate the feasibility of fusion as a source of energy. ITER will be the first fusion machine to produce net energy, which

Table 7.2: Bootstrap current model analysis comparing NEO simulation results with the Sauter model and the neural network model for a range of JET H-mode discharges. The values of the effective electron collision rate $\nu_{*e}$ and the carbon impurity fraction $f_I = z_I n_I / n_e$ are shown at the radial location of the center of the pedestal. The values for the Sauter model and the neural network model are the mean values in the core ($0 \leq \rho < 0.9$) and in the pedestal ($0.9 \leq \rho < 0.99$) of the percent discrepancy between the NEO result and the model, $100(1 - \langle j_\| B \rangle_{\rm model} / \langle j_\| B \rangle_{\rm neo})$.

| JET Shot # | $\nu_{*e}^{\rm ped}$ | $f_I^{\rm ped}$ | Core Sauter | Core NN | Edge Sauter | Edge NN |
|---|---|---|---|---|---|---|
| 075976 | 0.532 | 0.210 | 5.3% | 1.1% | 5.3% | 6.5% |
| 078682 | 0.560 | 0.236 | 3.2% | 2.1% | 10.9% | 3.1% |
| 075652 | 2.250 | 0.146 | 4.3% | 1.5% | 50.3% | 8.9% |
| 076678 | 2.395 | 0.153 | 6.9% | 2.5% | 33.2% | 10.2% |

means to produce and energy output higher that the input energy (approximately 10 times higher). Figure 7.5shows the size of the ITER tokamak. It is defined as an engineering meagproject.

There are two characteristics of the ITER tokamak that are particularly relevant to the present thesis. The first is that ITER will operate at higher temperatures (10-20 keV ) than DIII-D, which means in ITER the collision frequencies will be low, and essentially we will be in a low collisionality regime. The other characteristic is the high fraction of impurities that is expected in ITER . We should remember that the main improvements over the Sauter model of our new formula resides in the ion-impurity physics and the high collisionality regime. Our model handle many ions species and works well at low collisionality: this is a reason to believe that, for the ITER tokamak, the NN bootstrap current can be used as a model rather than the Sauter model. The principal issue the Sauter model will face is too many impurity species. A possible work that can be done for the ITER tokamak is to train a NN with ITER impurities datas. In our work we limited ourselves in a database with only carbon impurity. Be able to build a database with with ITER inputs and outputs, including impurities is the main stage to appply our formula to the ITER tokamak. We have seen during our research work that the coefficients $C_{Ta}$ and $C_{na}$ for the temperature and density scale lengths remain smooth when we change the impurity . This is not a surprise since NEO itself is capable of handling more than 6 impurity species.

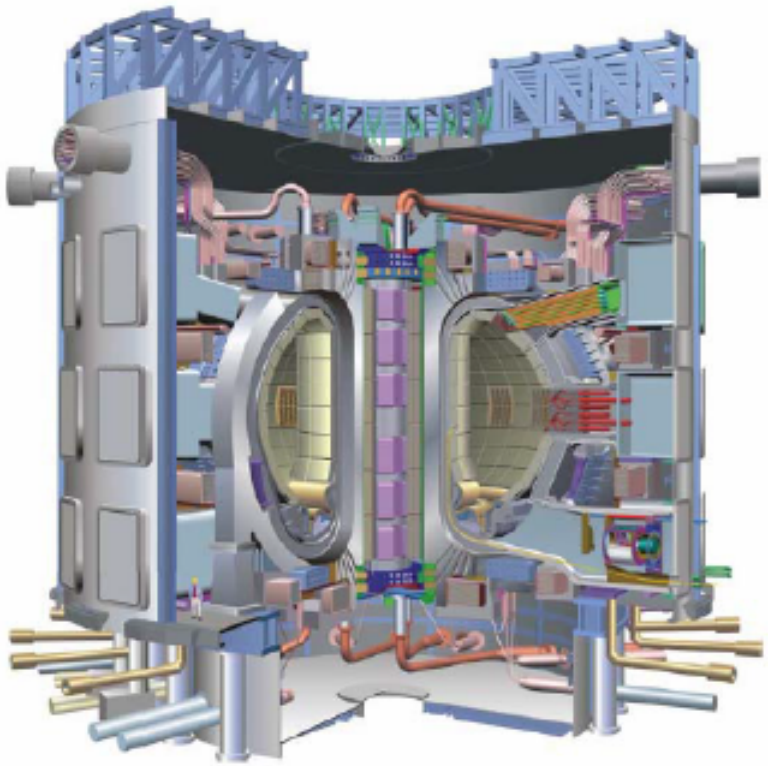

Figure 7.5: Rendition of the ITER design. To illustrate the colossal scale of the device, a person is shown standing on the lower left portion of the figure

# Chapter 8

# Applications of the new bootstrap current calculation

Since the introduction of this work, we tried to make clear that the bootstrap current not only can replace the inductively driven current but can have a much broader importance. It has an impact on both stability and confinement. Moreover since it is about 70-90% of the total current in the edge , it can be used in the current constraint for MHD equilibria reconstructions.

## 8.1 Implications for MHD equilibrium reconstructions

### 8.1.1 The Grad–Shafranov equation

The Grad–Shafranov equation is the equilibrium equation in ideal magnetohydrodynamics (MHD) for a two dimensional plasma or example the axisymmetric toroidal plasma in a tokamak. (We introduced the MHD equations in Chap.3) It is a two-dimensional, linear, partial-differential equation obtained from the reduction of the ideal MHD equations to two dimensions, often for the case of toroidal axisymmetry[41]. The equation :

$$\triangle^* \psi = -\mu_0 R^2 \frac{dp}{d\psi} - \frac{1}{2}\frac{dF^2}{d\psi} \tag{8.1}$$

Where $\psi$ is the flux function, $\mu_0$ is the magnetic permeability, $p(\psi)$ the pressure and $F(\psi) = RB_\phi$ , the magnetic field and current are given respectively by :

$$\vec{B} = \frac{1}{R}\nabla\psi \times \vec{e}_\phi + \frac{F}{R}\vec{e}_\phi \tag{8.2}$$

$$\mu_0 \vec{J} = \frac{1}{R}\frac{dF}{d\psi}\nabla\psi \times \vec{e}_\phi - \frac{1}{R}\triangle^*\psi\vec{e}_\phi \tag{8.3}$$

The elliptic operator $\triangle^*$ is :

$$\triangle^*\psi \equiv R^2\vec{\nabla}\cdot(\frac{1}{R^2}\vec{\nabla}\psi) \tag{8.4}$$

Many codes that reconstruct the equilibrium in the plasma solve the Grad-shafranov equation (Eq: 8.1). In particilar the EFIT code we used for our anaylsys [42]

efficiently solves for the equilibrium numerically by dividing $\psi = \psi_P + \psi_e xt$ into a plasma and an external component, $\psi_P$ and $\psi_e xt$ , separately computed using the differential and the integral forms of the equilibrium Eq: 8.1[43].

In an equilibrium reconstruction, the equilibrium Equation: 8.1 must be solved together with the available measurements as constraints on the plasma current source $J_\phi$. Figure 8.1 shows an example in DIII-D of the measurements techniques.

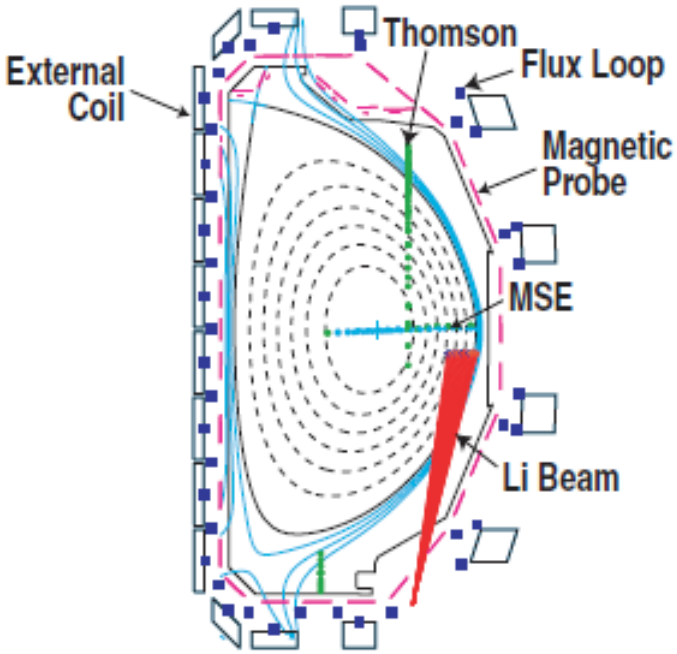


Figure 8.1: A cross section of DIII-D summarizing in one plane the locations of the external coils, external magnetic probes, flux loops, internal MSE, Li beam, and Thomson scattering kinetic profile diagnostics for the measurements.[42]

This is where comes the definition of the equilibrium parameter $\chi^2$:

$$\chi^2 = \sum i(\frac{M_i - C_i}{\alpha_i})^2 \tag{8.5}$$

where $M_i$ is the $ith$ magnetic measurement, $C_i$ is the comuted value at the $ith$ magentic measurement and $\alpha_i$ is the uncertainty associated with the $ith$ magnetic measurement.

Figure 8.2 shows a typical DIII-D tokamak reconstrcuted equilibrium using EFIT.

To study the potential applications of the new bootstrap current calculation on an MHD equilibrium reconstruction, we will use an extremely high collisionality DIII-D shot. In this shot the error associated with the Sauter model is very high. So it can be interesting to compare an equilibrium reconstruction with the Sauter and the NN bootstrap current as constraints. We use EFIT equilibrium solver, which uses external magnetic measurements and kinetic profile measurements. This example of an integrated modelling application between EFIT and NEO has been demonstrated for the first time in [2], using OMFIT [37].

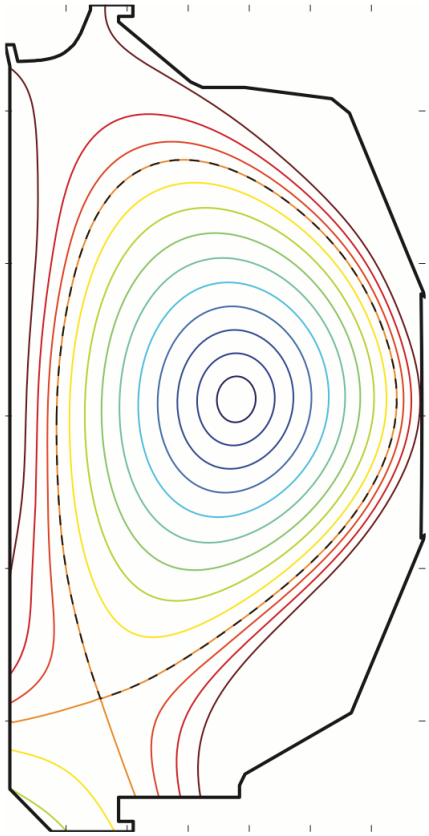

Figure 8.2: Contour plot of the square root of the toroidal flux, $\rho$, using the NN bootstrap current for the EFIT reconstruction.

In figure 8.3 it is shown the edge total current used as a constraint. In the same figure the value obtained for the EFIT reconstruction for this DIII-D case is also reported. What E. Belli *et al.* found during this exercise is that independently of the weight of the different constraints, the NEO bootstrap current is more consistent with magnetic measurements than the Sauter model, see [2]. To discuss quantitatively this result, let's remeber that the quantity $\chi^2$ that we already defined, provides a figure of merit for the accuracy of the fitted parameters and a larger $\chi^2$ in our case will mean that the computed bootstrap current is less consistent with magnetic measurements.

This exercise has shown that the NEO bootstrap current is more consistent with magnetic measurements than the Sauter model. The NEO bootstrap current constraint has led to lower $\chi^2$ values of the equilibrium reconstruction than the Sauter model: $\chi^2_{NEO} = 64.1$ and $\chi^2_{Sauter} = 85.0$. This is where the importance of our new model comes.Since the NEO model is a relatively slow model, it cannot be used to compute the bootstrap current current for equilibrium reconstruction in real time analysis nor integrated modeling applications. Figure 8.6 shows how much time NEO requires for a typical Boostrap current profile. The bootstrap current model ideal for these purposes is the NN bootstrap current model. The NN bootstrap current model is more accurate than the Sauter model and can be used in real time equilibrium reconstructions since it is also fast. On the same DIII-D high collisionality shot the NN bootstrap current has been used and has given $\chi^2_{NN} = 64.1$. This confirms the implication of our work on MHD equilibrium reconstructions. We have instrumented the workflow for equilibrium reconstructions in OMFIT to

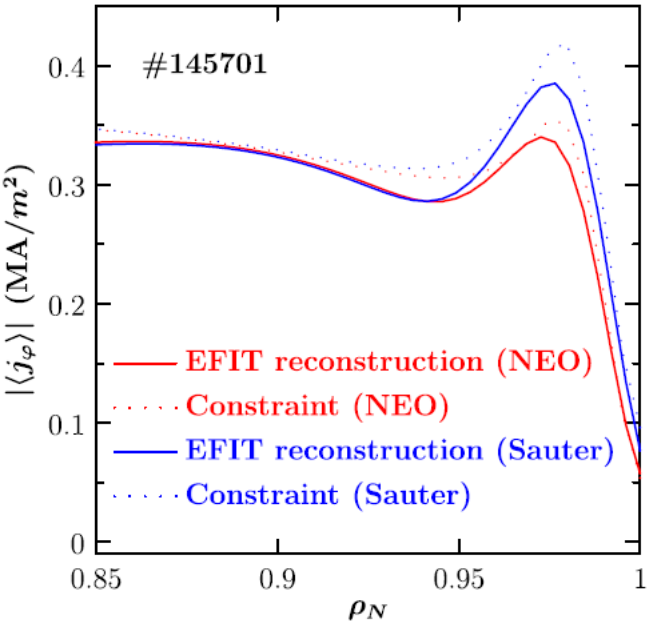


Figure 8.3: Comparison of the total toroidal currents in the edge with the NEO or Sauter current used as the bootstrap current model and embedded into the EFIT total current constraint.[2]

use the NN bootstrap current model. In figure 8.4 it is shown an example of current constraint for MHD equilibrium reconstruction. The dots represent the points where numerically computed values of the current are used. This is important since the bootstrap current is very difficult to measure and only models can provide values of the current there for the current constraint.

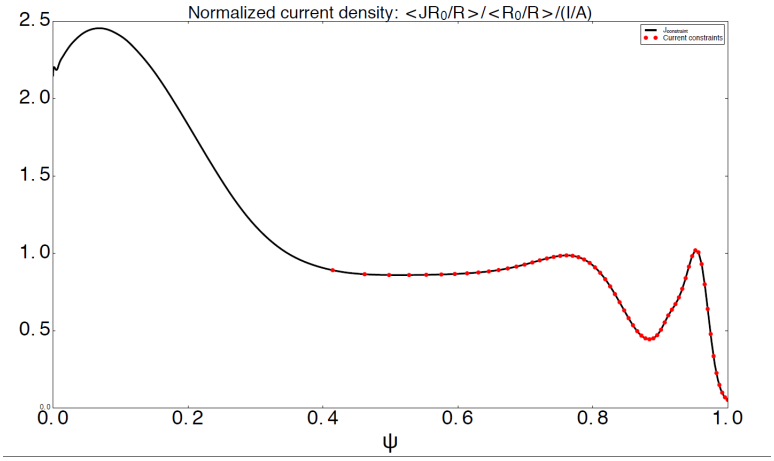


Figure 8.4: An example of current constraint for MHD equilibrium reconstruction

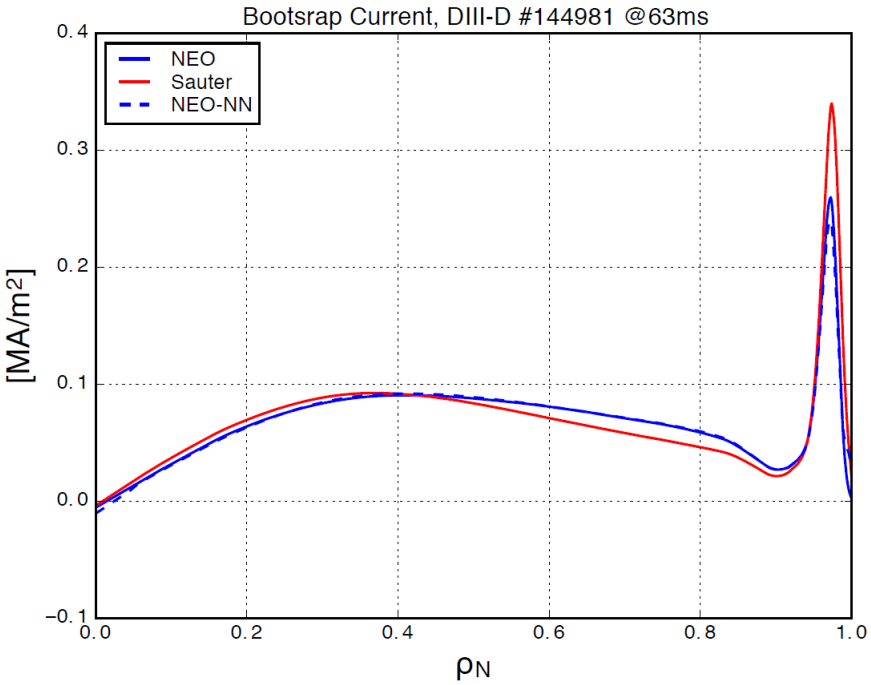


Figure 8.5: An example of a DIII-D high collisionality shot. The Sauter model largely overestimate the bootstrap current; the NN model has a much lower error with respect to NEO, especially in the edge, this is the reason why also the NN bootstrap current is more consistent with magnetic measurements and should be used for equilibrium reconstructions rather than the Sauter model

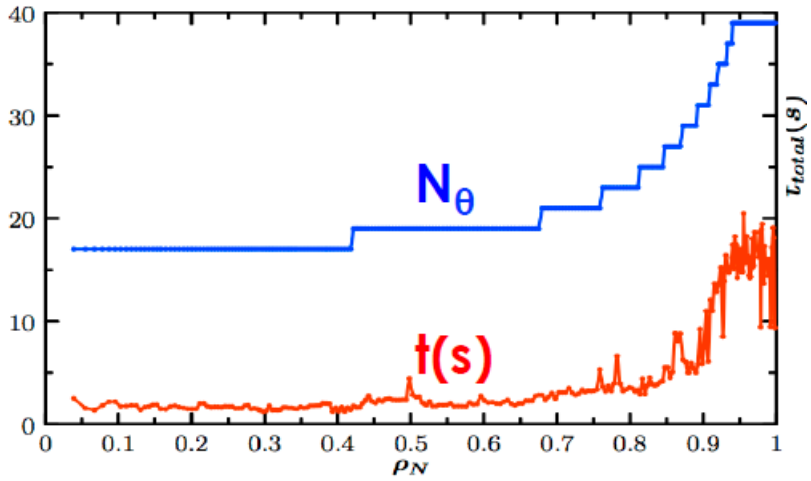


Figure 8.6: $N_\theta$ in blue is the number of poloidal points NEO uses in its computation. NEO increases the resolution towards the egde. In red is the time NEO uses at each radial point. In a 3 species plasma with 256 radial points NEO takes about 25min to compute the current profile.

# Chapter 9

# Conclusion

There is a particularly interesting consequence of the neoclassical transport in tokamak plasmas: the self-generated current called bootstrap current. The bootstrap current is that current which arises in toroidal plasmas driven by density and temperature gradients. This current is important for the study and the development of a steady state fusion reactor. A fast and accurate calculation of this current in the other hand is fundamental for integrated modelling applications such as MHD equilibrium reconstructions and pedestal structure predictions. Previous models to calculate the bootstrap current all had limitations: the Sauter model had the big disadvantage of being inaccurate especially at high collisionality regimes and in realistic multi-species plasmas; the NEO model offers a very accurate bootstrap current calculation through a numerical simulation, but as such takes too much time to compute a typical current profile (too much is with respect to real time analysis and integrated modeling purposes). We offered a new calculation of the bootstrap current based on a nonlinear multivariate regression using neural networks. This new calculation takes as inputs some dimensionless parameters that we carefully selected using analytic theory and exploring the physics mechanism behind the bootstrap current. Our new formulation not only has had an important improvement over the Sauter model in accuracy, but also, it only requires a few $CPU - \mu s$ to compute the current. Having the advantages of being fast and accurate, the new calculation is the ideal one to use for equilibrium reconstructions, as we have demonstrated in this work.Most importantly,our formula can be used in real time, while plasma experiments are taking place. We also have shown that our new calculation is not only applicable to the DIII-D tokamak where this research has been performed, but can easily be extended to other tokamak machines like JET where we also found very interesting results. Finally, we also have discussed the implication of this work for the for ITER, where the NN bootstrap current calculation would still be preferable to the previous one, because we handle in a better way the impurities in the plasma and we cover a broader range of collisionality regimes. The results of this thesis work have been well received in the fusion research community.The work has been successfully presented at the $59^{th}$ edition of the American Physical Society Division of Plasma Physics Meeting as well as at the DIII-D scientific meeting.Finally this work has been presented at the Swiss plasma center to scientists including Dr. Olivier Sauter who developed the previous formula receiving its positive feed-back.

# Bibliography


[1] M.C. Zarnstorff et al. "Bootstrap current in TFTR". In: *Phys. Rev. Lett.* 60.1306 (Mar. 1988).

[2] E.A. Belli et al. "Limitations of bootstrap current models". In: *Plasma Physics and Controlled Fusion* 56.4 (Mar. 2014).

[3] E.A. Belli and J. Candy. "Kinetic calculation of neoclassical transport including self-consistent electron and impurity dynamics". In: *Plasma Physics and Controlled Fusion* 50.9 (July 2008).

[4] O. Sauter and C. Angioni. "Neoclassical conductivity and bootstrap current formulas for general axisymmetric equilibria and arbitrary collisionality regime". In: *Physics of Plasma* 6.2834 (1999).

[5] O. Sauter and C. Angioni. "Erratum: "Neoclassical conductivity and bootstrap current formulas for general axisymmetric equilibria and arbitrary collisionality regime"". In: *Physics of Plasma* 9.5140 (2002).

[6] Q. Ren et al. "Test of bootstrap current models using high-$\beta_p$ EAST demonstration plasmas on DIII-D". In: *Plasma Physics and Controlled Fusion* 57.2 (Jan. 2015).

[7] O Meneghini et al. "Self-consistent core-pedestal transport simulations with neural network accelerated models". In: 57 (June 2017).

[8] Teobaldo Luda de Cortemiglia. MA thesis. Politecnico di Torino, 2016.

[9] Chigbo Mgbemene. "The effects of industrialization on climate change". In: (Sept. 2011).

[10] P.J. Mohr et al. *The 2014 CODATA Recommended Values of the Fundamental Physical Constants*. 2015. URL: `https://physics.nist.gov/cuu/Constants/index.html`.

[11] J.P. Freidberg. *Plasma physics and fusion energy*. Cambridge University Press, 2007.

[12] F.F. Chen. *Introduction to plasma physics and controlled fusion*. Springer,New York, 1984.

[13] T.J. Dolan. *Magnetic Fusion Technology*. Springer, 2013.

[14] F.L. Hinton and R.D. Hazeltine. "Theory of plasma transport in toroidal confinement systems". In: *Review of Modern Physics* 48.239 (Apr. 1976).

[15] P. Helander and D.J. Sigmar. *Collisional Transport in magnetized Plasmas*. Cambridge University Press, 2001.

[16] E.A. Belli and J. Candy. “Full linearized Fokker–Planck collisions in neoclassical transport simulations”. In: *Plasma Physics and Controlled Fusion* 54.1 (Dec. 2011).

[17] C.C. Hegna and J.D. Callen. “Interaction of bootstrap-current-driven magnetic islands”. In: *Physics of Plasmas* 4.1855 (1992).

[18] R.D. Carrera R.and Hazeltine. “Island bootstrap current modification of the nonlinear dynamics of the tearing mode”. In: *Physics of Fluids* 29.899 (1986).

[19] Kikuchi M. et al. “Bootstrap current during perpendicular neutral injection in JT-60”. In: *Nuclear Fusion* 30 (1990), pp. 343–355.

[20] M. Kikuchi et al. “Conceptual design of the steady state tokamak reactor (SSTR)”. In: *Fusion Engineering and Design* 18 (Dec. 1991), pp. 195–202.

[21] F. Najmabadi et al. “An advanced tokamak, advanced technology fusion power plant”. In: *IAEA-CSP–8/C). International Atomic Energy Agency (IAEA)* (2001), pp. 195–.

[22] Mitsuru Kikuchi. “A Review of Fusion and Tokamak Research Towards Steady-State Operation: A JAEA Contribution”. In: *Energies* 3 (Nov. 2010), pp. 1741–1789.

[23] S. Nishio et al. “Engineering aspects of a steady state tokamak reactor (SSTR)”. In: *Fusion Eng. Des* 15 (Nov. 1991), pp. 121–135.

[24] M. Kikuchi. “Steady state tokamak reactor based on bootstrap current”. In: 30.2 (1994).

[25] A.G. Peeters. “The bootstrap current and its consequences”. In: 42 (2000).

[26] R.D. Hazeltine. “Recursive derivation of drift-kinetic equation”. In: *Plasma Physics* 15 (Nov. 1973).

[27] M Kikuchi and M Azumi. “Experimental evidence for the bootstrap current in a tokamak”. In: *Plasma Physics and Controlled Fusion* 37.11 (1995), p. 1215. URL: `http://stacks.iop.org/0741-3335/37/i=11/a=003`.

[28] E.A. Belli and J. Candy. “Bootstrap current and neoclassical transport in tokamaks of arbitrary collisionality and aspect ratio”. In: *Physics of Plasmas* 4.9 (Sept. 1998).

[29] S. Koh et al. “Bootstrap current for the edge pedestal plasma in a diverted tokamak geometry”. In: *Physics of plasmas* 19.7 (July 2012).

[30] J. Candy and R.E. Waltz. “An Eulerian gyrokinetic-Maxwell solver”. In: *Journal of Computational Physics* 186.2 (Apr. 2003).

[31] G. Park et al. “Plasma transport in stochastic magnetic field caused by vacuum resonant magnetic perturbations at diverted tokamak edge”. In: *Physics of Plasmas* 17.102503 (Apr. 2010).

[32] K.H. Burrell and P.B. Osborne. “Quiscient H-Mode Plasmas with Strong Edge Rotation n the Cocurrent Direction”. In: *Physical Review Letter, American Physics Society* 102.155003 (Apr. 2009).

[33] C.G. Windsor et al. “A cross-tokamak neural network disruption predictor fot the JET and ASDEX upgrade tokamaks”. In: 45 (Apr. 2005).

[34] A. Murari et al. “New signal processing methods and information technologies for the real time control of JET reactor relevant plsams”. In: 86 (Nov. 2011).

[35] D.J.C. MacKay. *Information Theory, interference, and learning Algorithms*. Cambridge University Press, 2003.

[36] R.D. Hazeltine. “Rotation of a toroidally confined, collisional plasma”. In: *Physics of Fluids* 17 (1974).

[37] O. Meneghini et al. “Integrated modeling applications for tokamak experiments with OMFIT”. In: *Nuclear Fusion* 55.8 (2015), p. 083008. URL: `http://stacks.iop.org/0029-5515/55/i=8/a=083008`.

[38] E.A. Belli et al. “Eulerian Simulations of Neoclassical Flows and Transport in the Tokamak Plasma Edge and Outer Core”. In: *International Atomic Energy Agency (IAEA)* (2012).

[39] J. Candy and E. Belli. “GYRO Technical Guide”. In: *General Atomics Report GA-A26818,General Atomics* (Feb. 2011).

[40] M. Landreman and D.R. Ernst. “Local and global Fokker–Planck neoclassical calculations showing flow and bootstrap current modification in a pedestal”. In: *Plasma Physics and Controlled Fusion* 56.4 (Oct. 2012).

[41] H. Grad and H Rubin. “Hydromagnetic Equilibria and Force-Free Fields”. In: *Proceedings of the 2nd UN Conf. on the Peaceful Uses of Atomic Energy* 31 (1958), p. 190.

[42] L.L. Lao et al. “Reconstruction of current profile parameters and plasma shapes in tokamaks”. In: *Nuclear Fusion* 25.11 (1985).

[43] P.B. Snyder et al. “Magnetic Analysis of non-circular cross-section tokamaks”. In: *Nuclear Fusion* 22.813 (1982).